



**COMPARATIVE STUDY ON THE USE OF COHERENT RADAR-DERIVED
ELECTRIC FIELDS VS. STATISTICAL ELECTRIC FIELDS FOR THE
INITIALIZATION OF A HIGH-LATITUDE IONOSPHERIC MODEL**

THESIS

Christopher M. Hogue, Captain, USAF

AFIT/GAP/ENP/04-03

**DEPARTMENT OF THE AIR FORCE
AIR UNIVERSITY**

AIR FORCE INSTITUTE OF TECHNOLOGY

Wright-Patterson Air Force Base, Ohio

APPROVED FOR PUBLIC RELEASE; DISTRIBUTION UNLIMITED

The views expressed in this thesis are those of the author and do not reflect the official policy or position of the United States Air Force, Department of Defense, or the United States Government.

AFIT/GAP/ENP/04-03

COMPARATIVE STUDY ON THE USE OF COHERENT RADAR-DERIVED
ELECTRIC FIELDS VS. STATISTICAL ELECTRIC FIELDS FOR THE
INITIALIZATION OF A HIGH-LATITUDE IONOSPHERIC MODEL

THESIS

Presented to the Faculty

Department of Engineering Physics

Graduate School of Engineering and Management

Air Force Institute of Technology

Air University

Air Education and Training Command

In Partial Fulfillment of the Requirements for the

Degree of Master of Science (Applied Physics)

Christopher M. Hogue, BS

Captain, USAF

June 2004

APPROVED FOR PUBLIC RELEASE; DISTRIBUTION UNLIMITED

AFIT/GAP/ENP/04-03

COMPARATIVE STUDY ON THE USE OF COHERENT RADAR-DERIVED
ELECTRIC FIELDS VS. STATISTICAL ELECTRIC FIELDS FOR THE
INITIALIZATION OF A HIGH-LATITUDE IONOSPHERIC MODEL

Christopher M. Hogue, BS
Captain, USAF

Approved:

/signed/

1 June 2004

Clark M. Groves (Chairman)

date

/signed/

1 June 2004

David E. Weeks (Member)

date

/signed/

1 June 2004

Devin J. Della-Rose (Member)

date

Abstract

The structure and time development of the magnetosphere-ionosphere system have significant impacts on the Air Force and its mission. Specifically, an accurate knowledge of ionospheric plasma densities is important for the operation of many Air Force systems. This research analyzes plasma density structure development through comparing two distinct electric field models.

The two models compared here are a commonly used statistical model created by Heppner and Maynard [1987], and a more recently developed model using real-time coherent radar measurements from the SuperDARN radar network. Ionospheric simulations were run using Utah State University's Time-Dependent Ionospheric Model (TDIM) with the two electric field models as drivers, and density results from the simulations were compared with both a conceptual model and in-situ DMSP satellite measurements.

While there are limitations to the comparison technique, results indicate that, in general, using the SuperDARN-derived electric fields to drive the TDIM has advantages over using the statistical fields. The higher spatial and temporal resolution of the input electric fields generally seem to produce more realistic morphological density structures, with smoothing due to statistical averaging and geomagnetic index-binning reduced. This research provides an essential first step in using high resolution, real-time SuperDARN-derived electric fields to drive a physical model of the ionosphere in order to create realistic ionospheric density results.

AFIT/GAP/ENP/04-03

For Mike

Acknowledgments

I would like to express my deepest heartfelt appreciation to my wife for enduring my ranting about physics and for always helping me remember that home is where the heart is. My daughter is also responsible for this, as I can't help but smile and forget the rigors of thesis work when she giggles and says, "Hi Dada".

I also honor my parents, who developed in me the desire to love and to learn and who still today support my educational endeavors just as they have for so many years.

I would also like to express my sincere appreciation to my thesis advisor, Maj Clark Groves, for his friendship and support through this research effort. His previous work on this topic inspired me and the direction he provided through the entire effort always kept me on target. This work is as much his as it is mine, and I will be forever grateful for his help.

In addition, these acknowledgments would be incomplete without a huge thanks to my academic advisor, Maj Devin Della-Rose, for continuing to answer my thousands of ridiculous questions about physics which always made a 30 minute classroom discussion require 60 minutes of class time. Maj Della-Rose's patience and support through tough times leave me at a loss for adequate words.

I am also indebted to the many researchers who provided data, computer resources, and often guidance through this thesis work. Dr. Mike Ruohoniemi provided my initial vector through hours of explaining the particulars of SuperDARN and processing raw data files for our use in the study. Dr. Jan Sojka graciously provided the use of computer resources at Utah State University, and he also offered so much of his

valued time in one-on-one discussions about physical processes and modeling of the ionosphere. I will certainly never forget his professionalism and expertise. Michael David helped so much with keeping the computer resources working smoothly and providing much guidance on the finer points of the TDIM code. Also, special thanks to Dr. Marc Hairston at the University of Texas at Dallas for providing and explaining the finer aspects of the DMSP in-situ data, as well as NGDC and the ACE MAG instrument team from the ACE Science Center for providing geomagnetic and interplanetary datasets vital to the completion of this research.

Table of Contents

	Page
Abstract.....	iv
Dedication.....	v
Acknowledgements.....	vi
List of Figures.....	x
List of Tables	xii
I. Introduction	1
1.1. Problem Statement.....	1
1.2. Objective.....	3
1.3. General Approach.....	3
1.4. Air Force Impact.....	5
II. Background	7
2.1. Plasma Production	7
2.2. Plasma Loss	8
2.3. Plasma Transport	11
2.3.1. Horizontal $\mathbf{E} \times \mathbf{B}$ Drift.	11
2.3.2. Vertical $\mathbf{E} \times \mathbf{B}$ Drift.....	12
2.3.3. Neutral Wind-Induced Field-Aligned Air Drag.....	15
2.4. Time-Dependent Ionospheric Model (TDIM) Review	16
2.5. Input Model Review	19
2.5.1. Statistical Electric Field Model.....	21
2.5.2. NRL MHD-derived Electric Fields.....	25
2.5.3. Electric Fields from the AMIE Technique.....	28
2.5.4. SuperDARN-derived Electric Fields.	29
2.6. Previous Validation of SuperDARN E-fields.....	30
2.7. Previous Ionospheric Simulations Using Model E-fields.....	34
III. Methodology	37
3.1. Characterization of the Simulation Study Day	38
3.1.1. Solar Cycle, IMF Vector Data, and Geomagnetic Indices.....	38
3.1.2. Simulation Runtime Selection Criteria.	39
3.2. Interface between SuperDARN Data and the TDIM Model	46
3.3. Running the TDIM: Difficulties and Adaptations	53

3.4. Plotting Model Results.....	62
3.4.1. DMSP Satellite Availability.	62
3.4.2. Density Structures Valuable for Comparison Studies.	65
3.4.2.1. Low-Density Structures.	67
3.4.2.2. High-Density Structures.....	68
IV. Results and Conclusions.....	70
4.1. Results and Analysis.....	70
4.1.1. 0400 UT Results.	70
4.1.2. 1240 UT Results.	77
4.1.3. 1648 UT Results.	81
4.1.4. 2030 UT Results.	85
4.2. Conclusions and Possibilities for Future Work	86
Bibliography	91
Vita.....	95

List of Figures

	Page
1.1. Ionospheric Model Hierarchy	4
2.1. Typical Daytime Positive Ion Composition.....	9
2.2. Schematic of Mid- to High-Latitude Fields and $\mathbf{E} \times \mathbf{B}$ Drift	13
2.3. Schematic of a Classic Two-Cell Convection Pattern	14
2.4. TDIM Flux Tube Diagram.....	18
2.5. Heppner-Maynard Model BC Electric Fields	22
2.6. Heppner-Maynard Model DE Electric Fields	23
2.7. Heppner-Maynard Model A Electric Fields	24
2.8. Heppner-Maynard Rotationally Twisted Model BC Electric Fields	26
2.9. Heppner-Maynard Rotationally Twisted Model DE Electric Fields	27
2.10. North Geographic Region SuperDARN Sites.....	31
3.1. IMF and Geomagnetic Conditions of 23 February 2000	40
3.2. Convections Patterns of the Study Day	42
3.3. SuperDARN Grid Spacing.....	48
3.4. TDIM Grid Spacing	50
3.5. SuperDARN Data Interpolation Comparison	52
3.6. Turbulence Effects on TDIM Density Results.....	54
3.7. Inputs from an Uncoupled Auroral Flux Model	57
3.8. Enhanced Topside Auroral Density	59
3.9. Possible Fixes for the Erroneous Densities.....	61
3.10. DMSP F15 Satellite Track Example.....	66

4.1. DMSP-Model Comparison – 0400 UT	71
4.2. DMSP-Model Comparison – 1240 UT	72
4.3. DMSP-Model Comparison – 1648 UT	73
4.4. DMSP-Model Comparison – 2030 UT	74
4.5. Averaged Raw SuperDARN Velocity Data – 0400 UT	78
4.6. DMSP-Model Comparison – an Alternate Satellite Track at 1240 UT	80

List of Tables

	Page
1.1. Input Terms to the TDIM Physical Calculations	20

COMPARATIVE STUDY ON THE USE OF COHERENT RADAR-DERIVED ELECTRIC FIELDS VS. STATISTICAL ELECTRIC FIELDS FOR THE INITIALIZATION OF A HIGH-LATITUDE IONOSPHERIC MODEL

I. Introduction

1.1. Problem Statement

Knowing the condition of Earth's ionosphere globally at any single point in time is very difficult. While some parameters are observed by polar orbiting satellites at specific times throughout the day over certain locations, there are many locations and times that are left data-empty. Large and expensive radars have been built at many locations around the globe in the attempt to fill in some of this data-sparse area, but even these sensors leave information gaps, and they require certain ionospheric conditions in which to operate effectively. Electric fields are one increasingly important parameter that near-earth space physicists need to know in high resolution across the space and time system in Earth's ionosphere.

Many operational products used by the Department of Defense (DoD) community, among them High Frequency (HF) Illumination Maps and Global Positioning System (GPS) Estimated Single-Frequency Error Maps, are generated using electron density profiles derived from the Parameterized Real-time Ionospheric Specification Model (PRISM). However, PRISM itself is actually a suite of ionospheric

models. Ionospheric studies, and thus historical ionospheric model development, have typically been divided into three latitude regimes: the low-latitudes, the mid-latitudes, and the high-latitudes. PRISM was devised as a rapid look-up suite for ionospheric outputs from three distinct models, one from each latitude regime. For the high-latitudes (the focus of this study), PRISM is based on the outputs of a physical model of the ionosphere, the Utah State University (USU) Time-Dependent Ionospheric Model (TDIM). The TDIM is in-turn dependent on several inputs, one of which is electric fields. We will analyze the adequacy of these electric fields directly in the context of the physical model, TDIM, which underlies the PRISM suite.

Before proceeding, we must understand how the TDIM produces its output, and why a study of the adequacy of TDIM inputs is important. First, an electric field model generates the electric field. This E-field, along with auroral precipitation and thermospheric parameters provided from other models, is inputted into the TDIM, which is then used as the basis for the high latitude portion of PRISM. PRISM therefore generates its data from the results provided by the TDIM. A production model then uses the tables of data from PRISM to generate a suite of operational products, including the HF Illumination Maps and GPS Estimated Single-Frequency Error Maps. These end products are used to warn military assets of upcoming space weather that will affect their operations. As might be expected, small changes in the E-field input at the top “tier” of the model hierarchy can result in major changes to the products resulting at the end of the process, and errors can be costly. For example, an unexpectedly large error in GPS position may increase the risk of collateral damage during a missile attack, while an

unexpected HF blackout could cause a loss of communication between coordinating forces in a military operation. See Figure 1.1 for an illustration of this model hierarchy.

1.2. Objective

The broad objective of this research is to study deficiencies in the electric field models used to drive PRISM. We propose to address one targeted aspect of this general goal. While there have been extensive studies comparing E-field model results directly with E-field measurements, there have been fewer studies comparing a physical model's density simulations (based on different E-field model inputs) to in-situ measurements. We will attempt the latter, as it is the model's density results that lead directly to the resulting HF Illumination Maps and GPS Estimated Single-Frequency Error Maps and that are most-directly verified by satellite. A more complete DMSP Sensor discussion can be found in the methodology chapter. In addition, recent research has led to a theoretical method, in which first order two-dimensional ionospheric density structures can be derived through knowledge of just a few major parameters. This technique developed by Groves [2002] in his dissertation allows us to "verify" our model's final density results without the limitations that come with a satellite-model comparison study. Much detail concerning this will be discussed in the methodology and results chapters.

1.3. General Approach

In this research, two different E-field inputs into the TDIM have been used: the well-known and much-used statistical model developed by Heppner and Maynard [1987], and the Super Dual Auroral Radar Network (SuperDARN)-derived E-fields discussed by Greenwald et al. [1985]. These two E-fields, along with standard thermospheric and

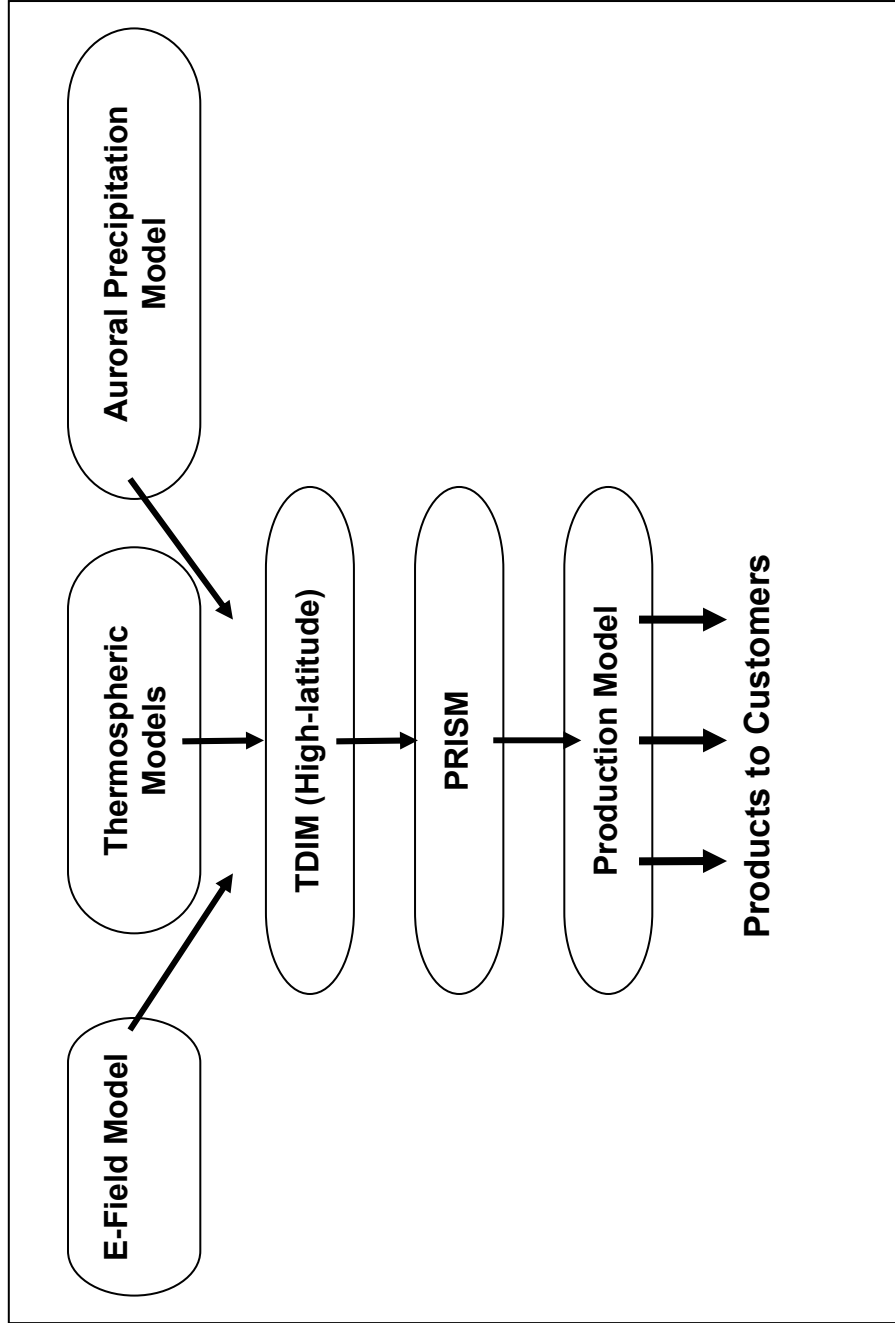


Figure 1.1. Ionospheric model hierarchy from the input models at the top of the diagram to the products at the bottom of the diagram. This research focuses on the electric field model input and the resulting TDIM output.

auroral precipitation models, were applied to the TDIM. Electron density maps created by the TDIM were compared against satellite in-situ density measurements and theoretical expectations. The results chapter contains the comparison between these outputs.

1.4. Air Force Impact

In general, the structure and time development of the magnetosphere-ionosphere system have significant impacts on the Air Force and its mission. Satellites traveling through the system depend upon the derived values of many atmospheric parameters in calculating the location of their orbit. An increase in neutral atmospheric density associated with higher geomagnetic activity will lead to increased thermospheric temperature and additional drag on the spacecraft. Higher energy particles within the plasma can also damage the satellite or lead to a loss of information being gathered or communicated by the satellite, and can endanger astronauts taking part in manned space missions. On the ground, changes in the ionosphere often lead to degradation or even loss of radio communications in use by all services in the Department of Defense. In an age of a total reliance by the military on communication technology, loss or degradation of these systems can lead to loss of many resources or even a service member's life. A quantitative understanding of how changes in solar activity lead to changes in Earth's ionosphere can help to prevent many of these negative impacts. Since adequately increasing direct observation of the vast magnetosphere-ionosphere (M-I) system is cost prohibitive and unlikely in the near-term, improvement of models depicting this system is of prime importance.

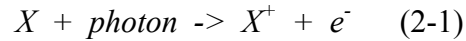
Specifically, an understanding of the adequacy of high-latitude electric field models as a driver for physical models of the ionosphere is critical for three major reasons. First, the high-latitude region represents the site of greatest coupling between the magnetosphere and the ionosphere. Greater understanding of the effects of electric fields in this region is a key to unlocking the important scientific question of M-I coupling. Second, high-frequency (HF) radars used in missile detection can receive false returns due to currently unforecastable density effects. Finally, plasma density affects the total electron content (TEC) of a column of the ionosphere. This TEC parameter is used in multiple operational models and uncertainty has far-reaching effects.

II. Background

Before discussing the specifics of the models used in this research and the results of running simulations using these models, we must first review a few key physical concepts that lead to some of the plasma density structures which develop in the ionosphere. The physical concepts are discussed in detail in many physics textbooks like Schunk and Nagy [2000]. The most important concept in this study is the balance among plasma production, loss, and transport in the high-latitude ionosphere.

2.1. Plasma Production

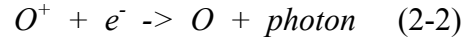
While there are many ways to produce plasma in the high-latitude ionosphere, the dominant production mechanism is photoionization. This is the process in which extreme ultraviolet radiation from the sun ionizes a portion of the Earth's neutral atmosphere forming electron-ion pairs, illustrated by equation 2-1 below.



This process occurs most strongly in the ionosphere's E-layer (altitudes from 120-150 km) and produces equilibrium E-layer plasma densities of approximately 10^5 cm^{-3} . In the auroral zone, these E-layer equilibrium densities can sometimes be increased by one order of magnitude by the ionizing effect of precipitating electrons from the Earth's magnetotail, especially when the IMF contains a southward component and the magnetosphere is "opened" to a portion of the solar wind's high-energy plasma.

2.2. Plasma Loss

The primary cause for plasma loss in the ionosphere is recombination of the ions and electrons back into neutral particles. This recombination occurs differently for atomic ions than it does for molecular ions. Atomic ions recombine directly to neutrals through a radiative recombination reaction like the one below:



Molecular ions recombine to neutral particles through dissociative recombination, illustrated by this example reaction:



Since the reaction rate for (2-2) is nearly 1000 times slower than for (2-3) [Schunk and Nagy, 2000], radiative recombination is not the dominant process by which the ionosphere loses atomic ions. Atomic ions can also be lost if they first experience an intermediate “ion-atom interchange” reaction, an example of which is shown here:



This reaction, which is far more common than radiative recombination, produces a molecular ion that can proceed through dissociative recombination. This extra step in the plasma loss process causes regions with mostly atomic ions to maintain a higher equilibrium plasma density, like in the F-layer, than regions where molecular ions dominate, like the E-layer. An illustration of this is contained in Figure 2.1. This is the case even though the E-layer has a larger plasma production rate through photoionization. Therefore, equilibrium plasma densities tend to be near 10^6 cm^{-3} in the high-latitude F region near an altitude of 300 km (commonly termed the “F-layer peak”).

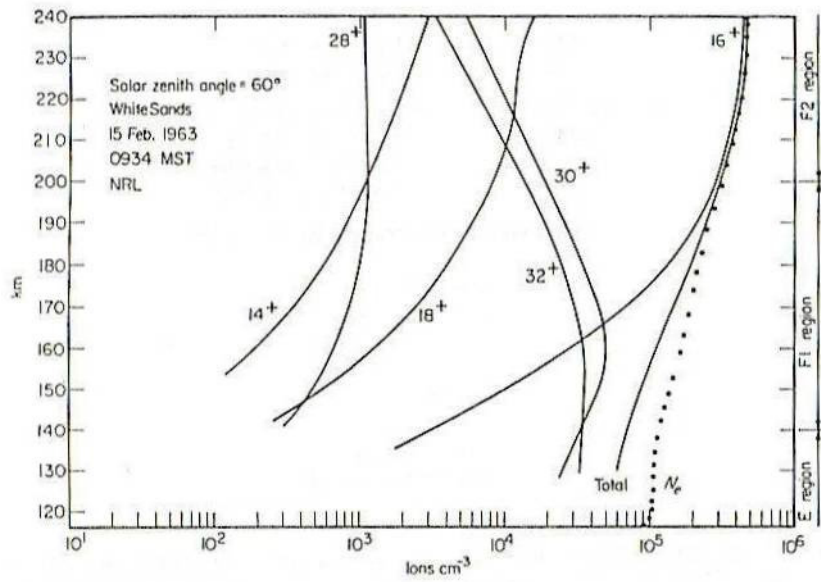


Figure 2.1. Typical daytime positive ion composition. Ionic mass numbers are shown, their probable identifications being 14^+ : N^+ , 16^+ : O^+ , 18^+ : H_2O (possibly a contaminant), 28^+ : N_2^+ , 30^+ : NO^+ , 32^+ : O_2^+ . The curve marked "Total" is the sum of all ion concentrations; the dotted curve marked N_e is the electron concentration profile determined from an ionogram. The solar zenith angle is near 60° [Holmes et al. 1965].

There is also an important process which can increase the local dissociative recombination rate in the F-layer of the ionosphere. During periods of enhanced geomagnetic activity, channels of strong electric fields can be created near the periphery of plasma convection cells. These relatively strong fields will accelerate the ions in the channel through $\mathbf{E} \times \mathbf{B}$ drift to much higher speeds than the surrounding plasma. Because of their neutrality and size, neutral particles do not react directly or quickly to the forcing mechanism. The resulting speed disparity between the ions and the neutral particles has two profound effects on recombination rates. First, frictional heating develops causing much higher plasma temperatures. According to Schunk et al. [1975], these high plasma temperatures increase dissociative recombination rates in the high-speed channel and thus increase the rate of plasma loss there. Second, the relative motion of the ions (mostly O^+ in the F-layer) compared to the neutrals (especially N_2 because of its large size) will markedly increase the ion-atom interchange reaction, or equation 2-4 above, since this reaction rate increases as the fourth power of the relative ion-neutral velocity [Schunk et al., 1975]. More ion-atom interchange reactions increase the “supply” of NO^+ , and will effectively increase dissociative recombination (equation 2-3) and thus further stimulate plasma loss in the F-layer. This plasma loss mechanism can effectively shift the balance of production/ loss/ transport in favor of plasma loss, especially during the disturbed geomagnetic conditions accompanying periods of strong southward turning in the IMF. Equilibrium plasma density, therefore, can decrease rapidly in these regions. One final note here is that as changes occur in the convection patterns, high-speed channels often shift as well. Movement of high-speed channels during the development of a geomagnetic storm can end up reducing plasma density across large areas in the storm-

time F-layer. These low-density structures are often recognizable in satellite observations and are therefore useful in studies such as ours here. We will discuss the resulting structures in the methodology chapter.

2.3. Plasma Transport

The final of the three key plasma processes essential in understanding the balance of plasma density in the high-latitude ionosphere is plasma transport. There are three dominant types of transport which play a role in the movement of plasma from region to region and from altitude to altitude. The three types are horizontal $\mathbf{E} \times \mathbf{B}$ drift, neutral wind-induced field-aligned air drag, and vertical $\mathbf{E} \times \mathbf{B}$ drift. As we will show, there are specific geomagnetic regimes and certain ionospheric regions where each of the types can dominate plasma balance in the high-latitude ionosphere.

2.3.1. Horizontal $\mathbf{E} \times \mathbf{B}$ Drift.

Plasma density does not merely reflect the balance of plasma production and loss over a localized area. Due to frequent forcing by convection electric fields, plasma originating over one area can drift to other areas. Depending on changes in the balance of forcing mechanisms at these locations, high-density plasma transported in this manner can sometimes move large distances before density depletion occurs. An example of this is when a convection electric field momentarily dips into a region of high plasma density. The high-density plasma is transported out of this region and perhaps into a region of relatively low density. If the convection then contracts back to higher latitudes, the high density plasma is left to co-rotate through surrounding lower density plasma until local equilibrium effects eventually reduce its density. This reduction may take much longer

than it took the high density plasma to move to this region. During strong geomagnetic storming, this effect is usually overshadowed by other effects, like increased plasma loss (perhaps through high-speed channels) or sometimes vertical transport.

2.3.2. Vertical $\mathbf{E} \times \mathbf{B}$ Drift.

Due to the earth's nearly vertical magnetic field structure in high latitudes, vertical $\mathbf{E} \times \mathbf{B}$ drift is sometimes overlooked as a significant plasma transport process in the high-latitude ionosphere. However, as discussed in detail by Groves [2002] in his dissertation, strong vertical $\mathbf{E} \times \mathbf{B}$ drift components can develop due to the decreasing dip angle of the magnetic field lines at increasing co-latitudes away from the magnetic poles. Since on large scales the electric and magnetic fields in the ionosphere are perpendicular to each other, $\mathbf{E} \times \mathbf{B}$ plasma drift can attain a significant vertical component. Due to the geometry displayed in Figure 2.2 from Groves [2002], vertical drifts can only develop where an east-west component of the electric field exists concurrently with non-vertical magnetic fields. The well-known equation describing this vertical drift is

$$V_{vert} = (E_{lat} \cos I) / B \quad (2-5)$$

where I is the angle of the magnetic dipole field away from horizontal. This means that mid- to high-latitude electric fields leading to plasma motion toward (away from) the pole will result in upward (downward) $\mathbf{E} \times \mathbf{B}$ plasma drift. Regions where upward vertical drift commonly occurs in a standard two-cell convection pattern are shown in Figure 2.3 with a lightly shaded circle. This region is commonly referred to as the “convection reversal”, as it is here that plasma in a standard two-cell pattern is redirected anti-sunward from its previous sunward trek in late morning and early afternoon. In this example, plasma will be affected by an upward forcing as it moves poleward along the

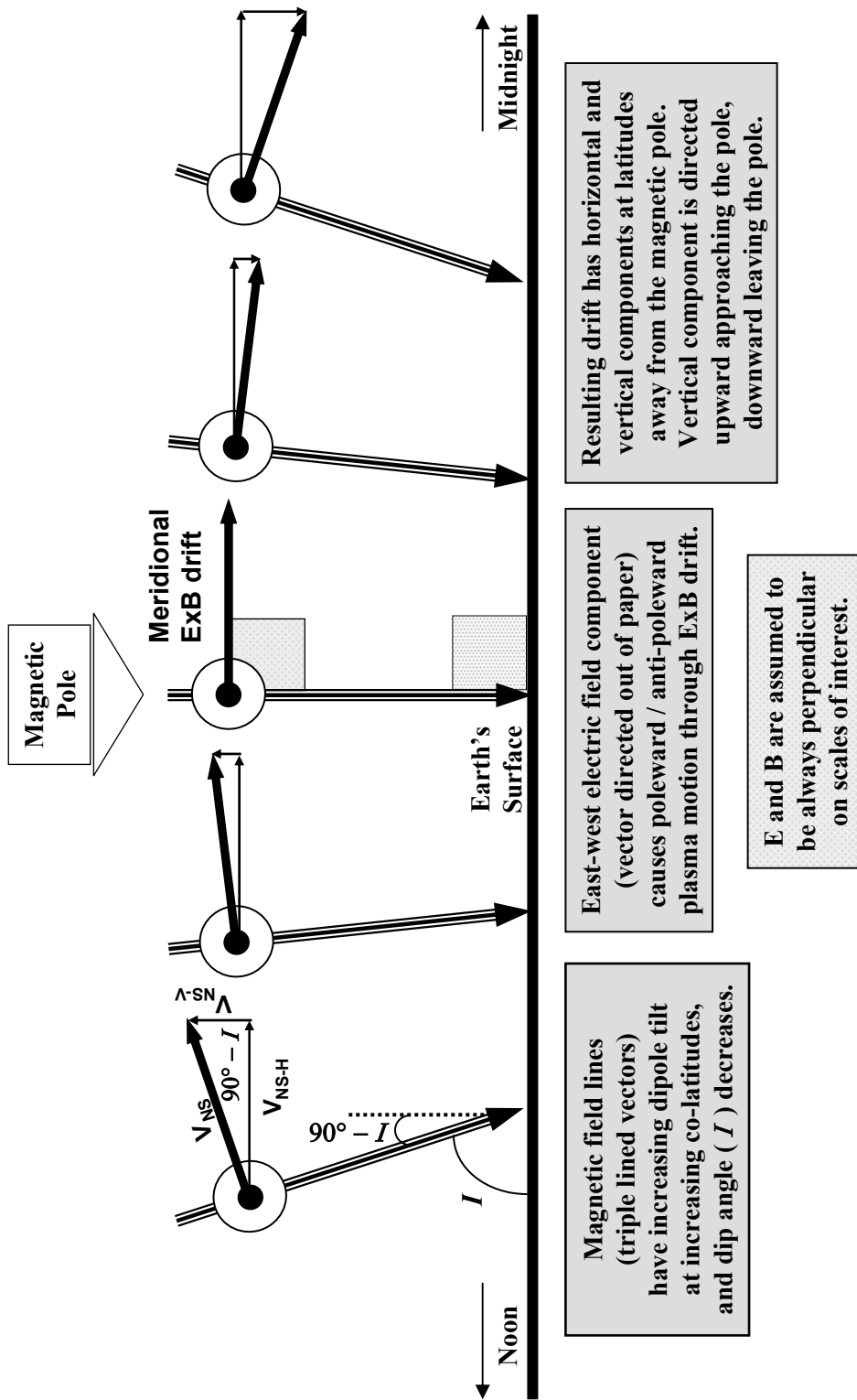


Figure 2.2. Schematic showing a 2-D cross section of the northern hemisphere mid- to high-latitude ionosphere along the noon-midnight meridian, illustrating the dip-angle effect [Groves, 2002].

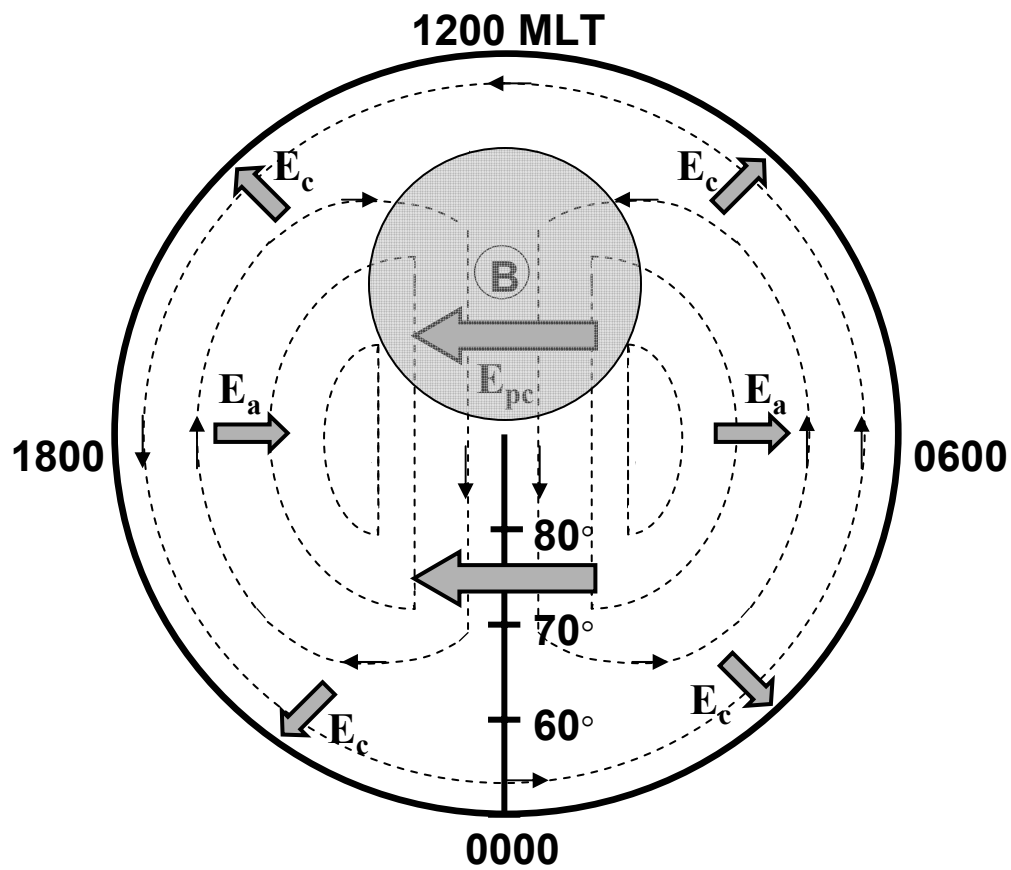


Figure 2.3. Schematic of northern hemisphere classic two-cell electric field potential pattern with primary mid- to high-latitude electric fields superimposed (large arrows). E_{pc} is the polar cap electric field, E_a is the auroral electric field, and E_c is the corotation electric field. The magnetic field is denoted by B . Resulting plasma flow due to $\mathbf{E} \times \mathbf{B}$ drift is shown with small arrows [Groves, 2002].

1200 Magnetic Local Time (MLT) meridian, have zero vertical forcing as it travels directly over the pole ($I = 90$ degrees), then be affected by downward forcing as it travels away from the pole.

The significance of vertical plasma motion is well understood. Upward plasma motion at altitudes above the height of the maximum density of the F2 layer (h_mF2 , normally near 300 km) should lead to enhanced densities, as the high density plasma from near the peak will be moved to regions of lower density above the peak. In addition, since recombination rates decrease at high altitudes due to the rapid decrease in neutral density, enhanced densities developed through vertical transport can remain for long periods. Downward plasma motion, conversely, will move plasma into regions of higher recombination rates, causing a loss of the plasma at these altitudes.

2.3.3. Neutral Wind-Induced Field-Aligned Air Drag.

The final transport mechanism we will discuss in this review is vertical air drag induced by neutral winds on the ions. This mechanism is based on a standard thermospheric principle: solar heating over the day-side forces a general day-to-night neutral wind flow. At high latitudes this flow moves over the pole, and is aligned with the noon-midnight meridional line, or alternately perpendicular to a standard dusk-dawn line. The closer a given flow vector is to the noon-midnight meridian, the more of a poleward component it will have. As a result, steady poleward-directed neutral winds will induce downward field-aligned air drag through neutral-ion drag forces, while anti-poleward neutral winds will induce upward field-aligned ion flow due to air drag. Since the ions are constrained to move along the field lines, this drag is only effective if there is a significant horizontal component of the dipole magnetic field where the flow occurs. This allows the ions to be

forced both in the horizontal direction of the neutral wind flow, and at the same time move down or up the field lines. Thus this effect is more pronounced the higher the colatitude, and is not present very near the pole, as vertical magnetic field lines will result in neutral particle motions which are perpendicular to possible ion movement. Still, even with significant horizontal B-field components, ion-neutral coupling is relatively weak compared to other forcing mechanisms on the ions. Thus, field-aligned flow is only significant if other forces acting on the ions are weak or absent. However, vertical motion of the plasma due to neutral wind-induced air drag has important effects on plasma density structure in certain regions as we will see later in this research.

2.4. Time-Dependent Ionospheric Model (TDIM) Review

Having now discussed basic concepts, it is important to review the models that will be used in this research. The Utah State University (USU) Time-Dependent Ionospheric Model (TDIM) was used in this work to simulate the effects of variable electric field inputs on computing global plasma density structure in the high-latitude ionosphere. Much success with similar studies comparing ionospheric forcing mechanisms gave us confidence in applying this model in our research as well. The two global electric field inputs into this ionospheric model were a statistically-based field created by Heppner and Maynard [1987] and a derived electric field based on plasma irregularity velocity measurements by the SuperDARN coherent scatter radar network (to be discussed in section 2.5). Since neither electric field dataset contains information on auroral precipitation or thermospheric properties (such as neutral winds and temperatures), statistical models are used as inputs for these parameters.

The TDIM ionospheric model was initially developed as a mid-latitude, multi-ion (NO^+ , O_2^+ , N_2^+ , and O^+) model by Schunk and Walker [1973]. The time-dependent ion continuity and momentum equations were solved as a function of altitude for a co-rotating plasma flux tube including diurnal variations and all relevant E- and F-region processes. This model was extended to include high-latitude effects due to convection electric fields and particle precipitation by Schunk et al. [1975, 1976]. A flux tube is followed as it moves in response to the convection electric fields, as shown in Figure 2.4. A further extension of the model to include the minor ions N^+ and He^+ , an updated photochemical scheme, and the mass spectrometer/incoherent scatter (MSIS) neutral atmosphere model is explained by Schunk and Raitt [1980]. The model was then extended to include ion thermal conduction and diffusion thermal heat flow by Schunk and Sojka [1982a], and the electron energy equation of Schunk et al. [1986] was added.

In addition to the chemistry and physics applied within the model, there are also some required inputs. As we illustrated in Figure 1.1, the main inputs for the high latitudes in the TDIM are convection electric fields, auroral precipitation, and thermospheric temperatures and winds. These inputs are traditionally statistical through the default use of Heppner-Maynard convection, Hardy et al. [1987] auroral precipitation, the MSIS-86 neutral atmosphere (temperature and composition) model [Hedin, 1987], and the HWM 90 neutral winds model generated by Hedin et al. [1991]. The Hardy et al. [1987] auroral precipitation statistical model is based on data gathered from many satellite passes, then averaged and binned as a function of magnetic location and geomagnetic activity as measured by 3-hourly Kp. The auroral characteristics were determined for each whole number value of Kp from 0 to 5 and for Kp ≥ 6 -. The

Heppner-Maynard statistical convection model, discussed in detail in the next section, was quantitatively identified and interfaced with the TDIM using the analytical functions developed by Rich and Maynard [1989]. As we used a different input for the convection electric field, we had to create the proper spatial/time interface so that SuperDARN data could be used by the TDIM. This will be explained fully in the methodology chapter. Table 1.1 created by Sojka [1989] provides a detailed description of the input terms for TDIM's computations. In this paper, Sojka contends that the model is most sensitive to changes in the convection electric field and auroral precipitation inputs, especially during disturbed geomagnetic conditions where fine scale structure and rapidly changing E-fields and aurora are the rule and tend to dominate the chemistry and transport mechanisms in the high-latitude ionosphere.

2.5. Input Model Review

The electric fields discussed in this research are the statistically-derived fields [Heppner and Maynard, 1987], the Naval Research Lab (NRL) Magnetohydrodynamics (MHD) Model fields extensively described by Fedder and Lyon [1995], the E-fields derived by the AMIE technique described by Richmond and Kamide [1988] and Richmond [1992], and the E-fields derived using observed data from the SuperDARN coherent scatter radars. Our research comprises only a comparison of TDIM-Statistical runs with TDIM-SuperDARN runs. However, we discuss the MHD Model and the AMIE technique E-fields since prior TDIM simulations use these electric field drivers, and we will compare our findings to the findings of those researchers.

Table 1.1. Input terms to the TDIM physical calculations [Sojka, 1989].

Continuity Equation Inputs		
<i>Term</i>	<i>Process</i>	<i>Model Representation and Inputs</i>
Production	solar EUV	empirical Solar spectrum (F10.7 index); empirical neutral atmosphere (MSIS) (F10.7 and <i>ap</i>)
	solar resonantly scattered radiation	adopted ionization cross sections; distribution of resonantly scattered radiation; adopted ionization rate profiles
	auroral precipitation	empirical distribution of precipitating electrons; their flux and energy (statistical models (<i>Kp</i> or <i>AE</i>) or images); adopted semiempirical ionization rate profiles
Loss	recombination	comprehensive chemistry scheme; ion and electron temperature-dependent reactions (energy equation); neutral atmosphere (MSIS) (F10.7 and <i>ap</i>)
	composition changes	ion chemistry (NO^+ , O_2^+ , O^+ , N_2^+ , N^+ , and He^+); temperature-dependent reactions (energy equation); neutral atmosphere (MSIS) (F10.7 and <i>ap</i>)
Diffusion	transport	momentum equation
Momentum Equation Inputs		
<i>Term</i>	<i>Process</i>	<i>Model Representation and Inputs</i>
Horizontal transport	$(\mathbf{E} \times \mathbf{B})/B^2$	magnetic field (eccentric dipole); empirical magnetospheric electric fields (IMF and <i>Kp</i> dependent); empirical equatorial dynamo electric field model; corotational electric field in magnetic frame
Vertical transport	induced drifts	vertical component of $\mathbf{E} \times \mathbf{B}/B^2$ (same inputs as for horizontal transport); empirical neutral wind model to induce vertical drift.
Pressure	pressure gradient	ion density and temperature (continuity and energy equations)
Stress tensor	E-induced stress	ion-neutral collision frequencies; neutral atmosphere (MSIS) (F10.7 and <i>ap</i>)
Momentum transfer	collisions	adopted collision frequencies; neutral atmosphere (MSIS) (F10.7 and <i>ap</i>); neutral wind model; ion temperatures (energy equation)
Gravity	acceleration	adopted radial inverse square gravitational acceleration
Energy Equation Inputs		
<i>Term</i>	<i>Process</i>	<i>Model Representation and Inputs</i>
Heat source	volume heating rate	solar heating rate model; semiempirical auroral particle rate model; joule heating, ion-neutral drifts; continuity and momentum equations; neutral atmosphere (MSIS) (F10.7 and <i>ap</i>)
Heat sinks	volume cooling rate	cooling rates for collisions with electrons, ions, and neutrals (continuity equation); neutral atmosphere (MSIS) (F10.7 and <i>ap</i>)
Energy exchange	collisions	ion/electron/neutral collision frequencies; ion velocities (momentum equation); neutral wind model; densities (MSIS) (continuity equation)
Heat flow	heat flow	upper boundary heat flux ("guessed")
Pressure	transport	momentum equation
Stress tensor	transport	momentum equation

2.5.1. Statistical Electric Field Model.

The statistical electric fields were created by averaging large volumes of ionospheric field data observed by the Dynamics Explorer (DE) 2 satellite under specific interplanetary magnetic field (IMF) conditions. The parameters used to separate the datasets are the IMF orientation and the Kp magnetic index. Heppner and Maynard [1987] showed that with a southward Bz component of the IMF, the electric field pattern (and thus the ionospheric convection pattern) usually forms in one of three models, which they term model BC, model A, and model DE. All three models are a version of the classic two-cell convection pattern believed to exist during periods of southward Bz. Each pattern is defined for an average Kp magnetic index of 3+ to 4-. An increase or decrease in Kp scales the strength of the resultant electric field. This means that increasing the Kp index (or geomagnetic “storminess”) will increase the potential difference in the E-field pattern and will tend to move the equatorward boundary of the convection field to lower latitudes. Conversely, lowering the index will weaken and contract the convection pattern. Each of the basic models is illustrated in Figures 2.5, 2.6, and 2.7. The BC model in Figure 2.5 represents the pattern formed with a positive By component (in GSM coordinates) in the geographic northern hemisphere (i.e., the geomagnetic *southern* hemisphere). Conversely, the BC pattern in the geographic southern hemisphere (the geomagnetic *northern* hemisphere) requires a negative By component. The DE Model in Figure 2.6 represents the pattern formed with a strong negative By component in the northern geographic hemisphere (positive in the south). The A Model in Figure 2.7 is the transitional model between the two and represents a relatively weak negative By component in the northern geographic hemisphere.

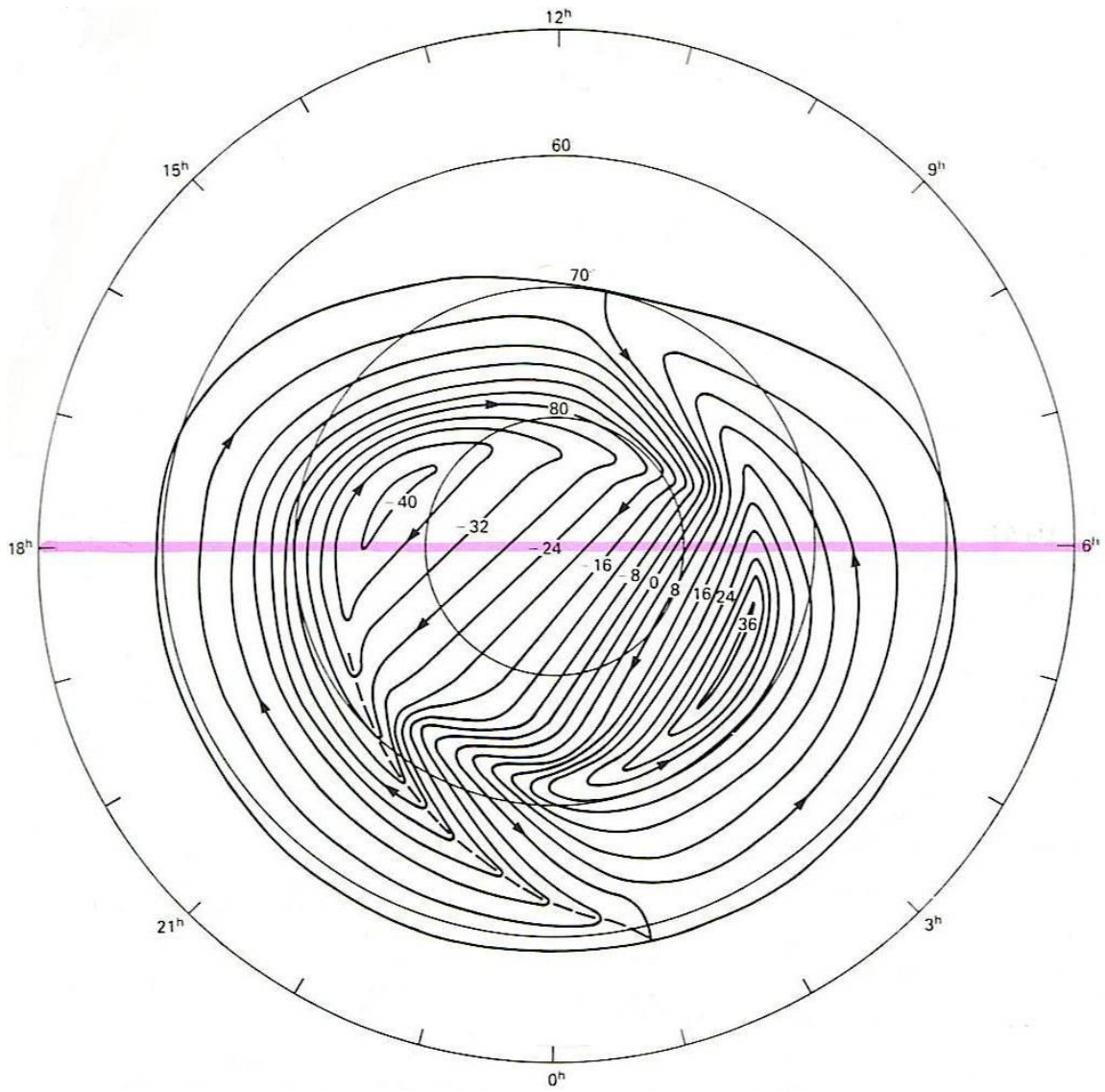


Figure 2.5. Equipotential contours representing the Heppner-Maynard model BC electric field pattern. The arrows correspond to resulting plasma motion [Heppner and Maynard, 1987].

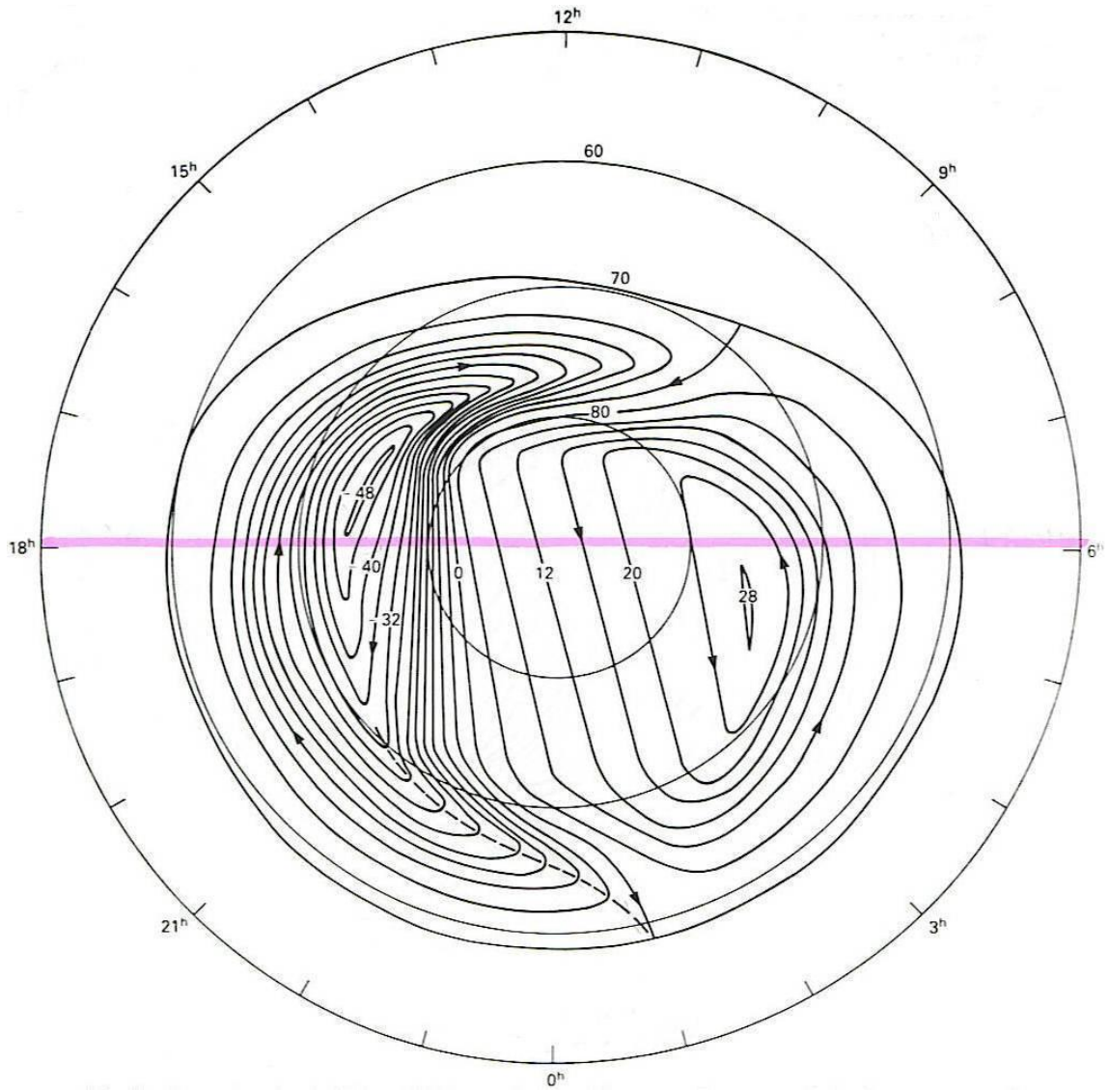


Figure 2.6. Equipotential contours representing the Heppner-Maynard model DE electric field pattern. The arrows correspond to resulting plasma motion [Heppner and Maynard, 1987].

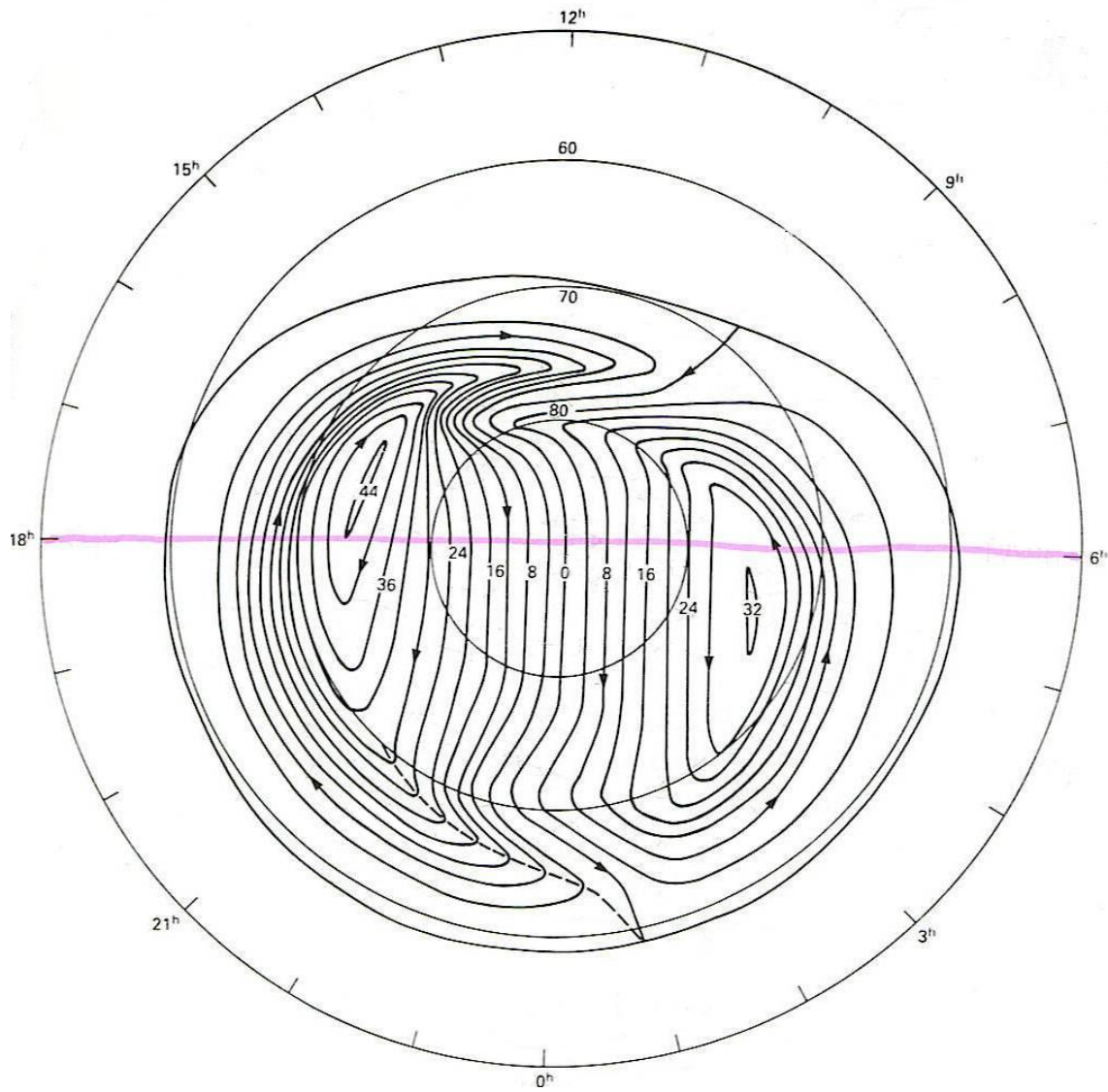


Figure 2.7. Equipotential contours representing the Heppner-Maynard model A electric field pattern. The arrows correspond to resulting plasma motion [Heppner and Maynard, 1987].

For instances of a positive B_z component, Heppner and Maynard provide rotationally twisted two-cell convection models based on the B_z southward patterns described above. It is in these northward B_z IMF configurations that there is the most uncertainty among many ionospheric researchers. A weak magnetosphere-ionosphere coupling during B_z northward conditions tend toward weak and varied convection patterns, thus creating a challenge for statistical models [Bristow et al., 1998]. The two variations provided by Heppner and Maynard are included here as Figures 2.8 and 2.9. Figure 2.8 illustrates the rotational twisting of model BC when the IMF B_z is weakly (left) and strongly (right) positive. Figure 2.9 shows the distorted configuration of the DE model under these same B_z conditions.

These visual Heppner-Maynard model convection patterns have been translated to code for entry into ionospheric computer models by analytical functions developed by Rich and Maynard [1989]. As we noted earlier, when this statistical E-field is used as input into TDIM, we must also specify an independent source for auroral flux, neutral winds, and other thermospheric quantities.

2.5.2. NRL MHD-Derived Electric Fields.

The Naval Research Laboratory (NRL) MHD Magnetosphere model has been discussed in detail by Fedder and Lyon [1995] and Fedder et al. [1995a]. Two sub-components of this model are a set of self-consistent ionospheric electric field patterns and auroral precipitation values. As we discuss later, these have been used as an input to the TDIM. Of specific importance when discussing the model's use as an input to an ionospheric model is how its values at the inner boundary (3.5 Earth radii) are determined. The model derives its values by solving the ideal MHD equations for the

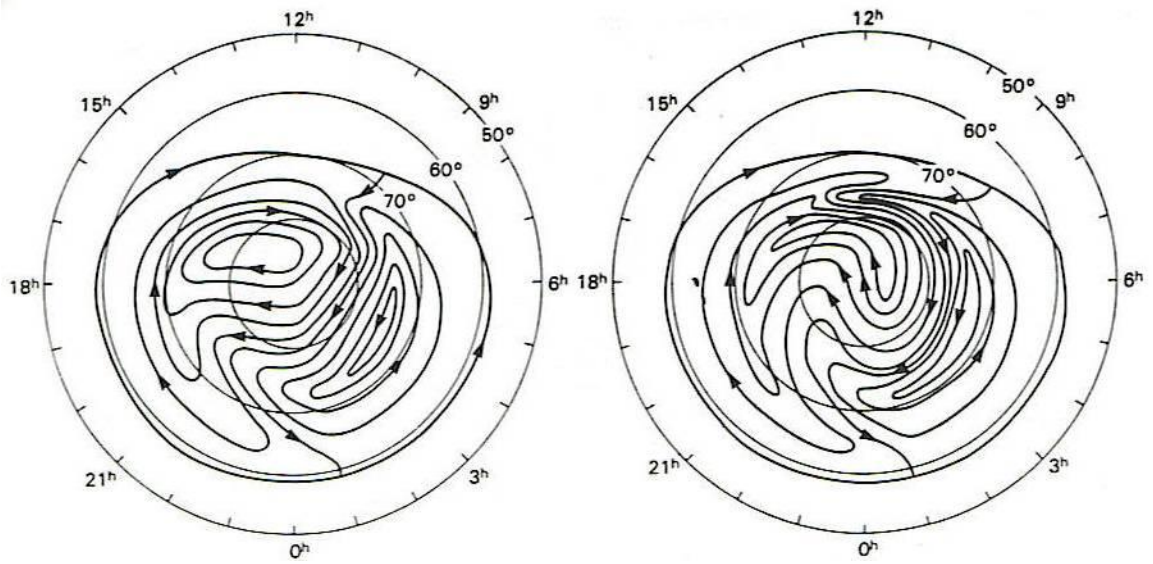


Figure 2.8. Equipotential contours representing the Heppner-Maynard rotationally twisted model BC electric field pattern. The arrows correspond to resulting plasma motion [Heppner and Maynard, 1987].

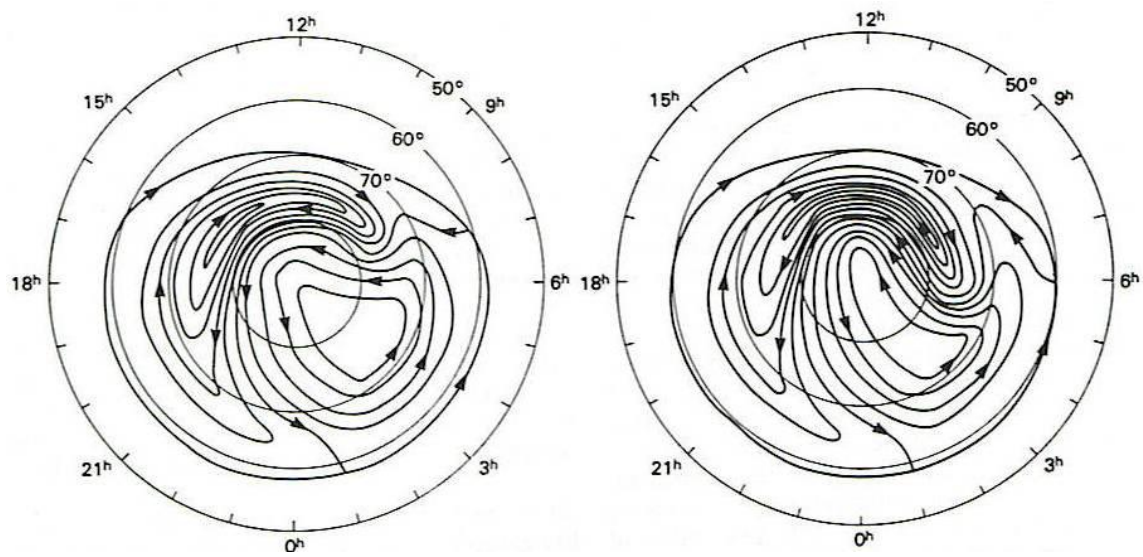


Figure 2.9. Equipotential contours representing the Heppner-Maynard model DE electric field pattern. The arrows correspond to resulting plasma motion [Heppner and Maynard, 1987].

solar wind and the outer magnetosphere (beyond $3.5 R_E$). The nonorthogonal adapted mesh used by the model maximizes the spatial resolution at the magnetopause, in the ionosphere, and in the geomagnetic tail. Its fine temporal resolution of less than 1 second allows the model to describe unambiguously the propagation of fast waves on the mesh. Fedder and Lyon [1987] have shown the model simulates the important process of magnetic merging in such a way that the reconnection rate is determined by the physical conditions of the solar wind and the conductivity of the ionosphere, with the simulated reconnection rate being insensitive to the mesh size. Fedder et al. [1995b] developed the ionospheric conductance by using a parameterized empirical model of both the solar EUV and auroral precipitation ionization sources. Parameters from the innermost mesh points are used to determine the field-aligned electric potential, which leads to the characteristic energy of the precipitating electrons and flux from the field-aligned current. Sojka et al. [1997] describe this process in detail.

2.5.3. Electric Fields from the AMIE Technique.

The Assimilative Mapping of Ionospheric Electrodynamics (AMIE) procedure, described by Richmond and Kamide [1988] and Richmond [1992], combines statistical models and data from a variety of selectable ground- and space-based magnetic and plasma sensors in four separate least square fitting solutions [Richmond, 1992; Emery et al., 1996] to find the auroral energy flux, the average auroral electron energy, the Pedersen and Hall height-integrated conductances, and the electric potential, currents, and other electrodynamics [Slinker et al., 1995]. Data can be input from magnetometers, radars (coherent and incoherent), DMSP ion drift meter (IDM) sensors, and satellite-based UV imagers to name just a few. As we will discuss with the SuperDARN model

output, statistical models are used to constrain the mapped patterns of electrodynamic parameters over data-sparse regions. The procedure first adjusts the statistical starting point for height-integrated conductance and auroral precipitation using data from available satellite datasets. The updated conductance map is then applied to the magnetic perturbation data from ground magnetometers to affect the statistical convection patterns. Radar-derived and satellite-observed plasma motion can also be assimilated to exact a solution. Opportunity for error can be quantified and used to adjust the weighting factor for the data observed by each sensor. This error can be caused by observational error, errors associated with AMIE's inherent spatial smoothing, and errors connected to inaccuracies in the simplifying assumptions used within the procedure.

2.5.4. SuperDARN-Derived Electric Fields.

The source of the electric field we will use for comparison against the statistical Heppner-Maynard field is derived by a network of radars commonly referred to as SuperDARN. The Super Dual Auroral Radar Network currently contains nine HF coherent scatter radars in the northern hemisphere (and six in the southern hemisphere) positioned near the 60 degree invariant latitude. This network of radars provides a measurement, when ionospheric irregularities are present, of the two-dimensional $\mathbf{E} \times \mathbf{B}$ plasma drift in the high-latitude ionosphere. Real-time data measured by each radar are averaged into two-minute blocks, and are available via the internet within a few minutes via communication links [Ruohoniemi et al., 2001]. Since each radar can only measure one-dimensional (line of sight) velocities, two radars whose fields of view overlap must sample the same plasma to resolve independent vector components. While an effort is made to space the radars equally around the high latitudes, the international political

environment has led to a relative scarcity of radars (and thus data sparseness) in the far eastern geographic longitudes, while substantial coverage exists in the European and North American high-latitudes from the Scandinavian countries west to the Alaskan coastline. See Figure 2.10 for an illustration of radar locations and their respective coverage areas. In areas of low data coverage, radar-determined potential data are fitted with data from a statistical e-field model produced by Ruohoniemi and Greenwald [1996] at the Johns Hopkins University (JHU) Applied Physics Laboratory (APL). This is accomplished through a spherical harmonics fitting discussed by Ruohoniemi and Baker [1998], where the coefficients of the spherical harmonics functions are such that the solution is constrained by statistical potential values in data sparse regions. While one may be concerned that the statistical pattern would improperly shape the real-time radar-derived data, Shepherd and Ruohoniemi [2000] showed that with ample radar measurement coverage – especially in the region between the polar cap potential maxima – the general solution for the global convection pattern is nearly independent of the choice of statistical model. This leads to a greater level of comfort in case studies using data collected during high-coverage periods. Again, as with statistical model E-fields, the SuperDARN E-field stands alone and is independent of any thermospheric and auroral input. Other input models must be selected to characterize these parameters when running the TDIM.

2.6. Previous Validation of SuperDARN E-fields

Having discussed the historic electric field patterns used for TDIM ionospheric simulations, we will now discuss in greater detail the model used in this research.

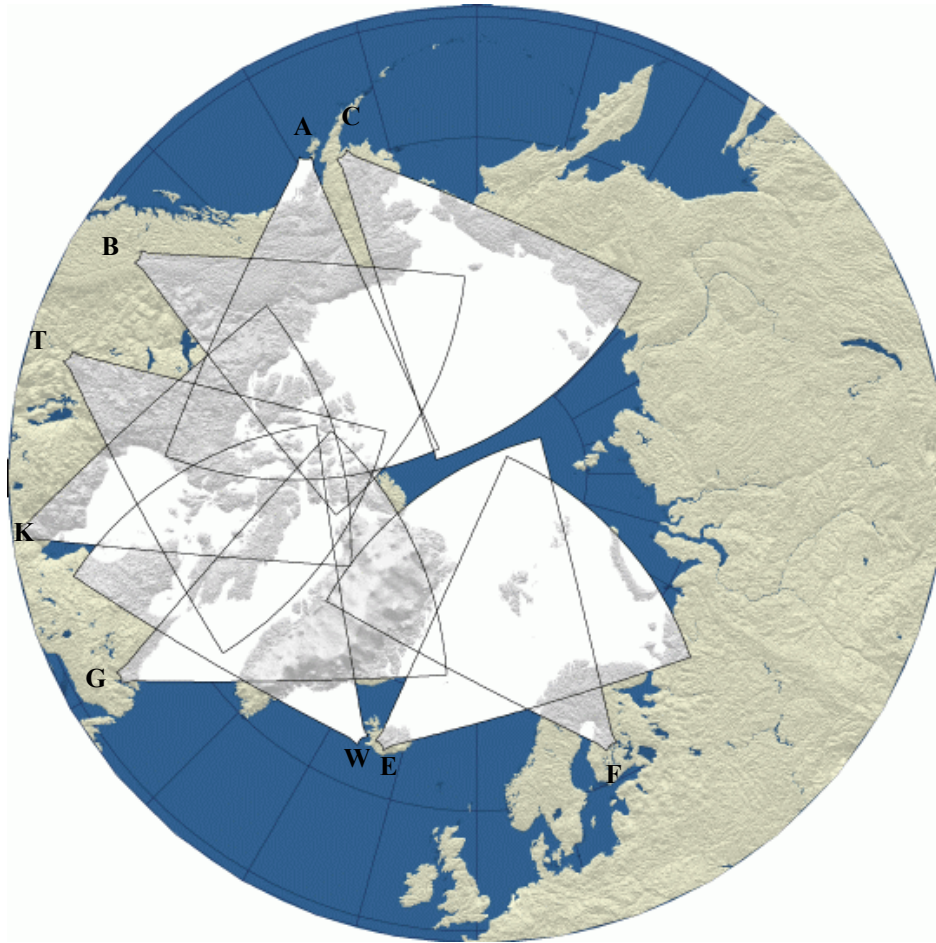


Figure 2.10. North Geographic Polar Region SuperDARN sites [superdarn.jhuapl.edu].

South Magnetic Polar Region SuperDARN sites

<u>King Salmon</u>	C	Operated by the <u>Communications Research Laboratory</u> in Japan.
<u>Kodiak</u>	A	Operated by the Geophysical Institute, UAF in the USA.
<u>Prince George</u>	B	Operated by the <u>Univ. of Saskatchewan</u> in Canada.
<u>Saskatoon</u>	T	Operated by the <u>Univ. of Saskatchewan</u> in Canada.
<u>Kapuskasing</u>	K	Operated by the <u>JHU/APL</u> in the USA.
<u>Goose Bay</u>	G	Operated by the <u>JHU/APL</u> in the USA.
<u>Stokkseyri</u>	W	Operated by <u>CNRS/LPCE</u> in France.
<u>Þykkvibær</u>	E	Operated by the <u>Radio and Space Plasma Physics Group, Univ. of Leicester</u> in the UK.
<u>Hankasalmi</u>	F	Operated by the <u>Radio and Space Plasma Physics Group, Univ. of Leicester</u> in the UK.

Throughout the development of the SuperDARN coherent radar network in the 1980's and 1990's, many validations of the resulting radar-derived potential maps and convection patterns were accomplished. Early in this development period, when only a few of the radars in the spatial network existed, two-dimensional velocities could not be unambiguously resolved, as each radar can independently measure only line-of-sight velocities (toward and away from the transmitter). In these cases, a procedure was developed to use the full scan width of a single radar to resolve two-dimensional velocities. This procedure required slowly changing ionospheric conditions (both stable and uniform flow), and therefore a stable or slowly changing IMF. A larger-scale convection pattern was inferred by noting that the convection velocity must everywhere be divergence-free. Ruohoniemi et al. [1989] describe this technique in detail and use it to discuss plasma flow characteristics observed in high-latitude areas, such as the convection-reversal region near magnetic midnight, L-shell-aligned flow in the dusk sector, and counterstreaming in the dayside cleft.

Later in the development period, as more radars were added to the network, pairs of radars with common coverage areas were used to unambiguously resolve two-dimensional flow. Since the pattern is obtained in fine temporal resolution (2 min), studies could be performed examining fluctuating ionospheric conditions and fine-scale flow structures that formed within these conditions. Greenwald et al. [1995] use this technique to discuss characteristics of plasma flow obtained from two Canadian radar sites as the orientation of the IMF evolved from a large positive B_y to a small positive B_y , all during steady northward B_z conditions. These observed convection characteristics were compared to previously defined statistical patterns by Heppner and

Maynard [1987] and others for this same IMF configuration, and differences were noted. While these studies made the ionospheric research community aware of SuperDARN's expanding capabilities, a relatively short history of archived data prevented a statistical compilation of observed convection patterns.

In the mid 1990's, an ever-increasing set of archived SuperDARN data allowed the creation of a new statistical model using data compiled by the SuperDARN radar located at Goose Bay, Labrador, over the period September 1987 to June 1993. Ruohoniemi and Greenwald [1996] explain that the parameters used to separate the patterns are IMF direction in the GSM y-z plane and the total B-field magnitude. The directionality of the IMF is separated into eight bins, one for each of the eight main directions around the y-z dial. The total magnitude of the IMF is separated into three intervals: less than 4 nanoteslas (nT), 4-6 nT, and 6-12 nT. The result of this study was that the patterns created through statistical analysis matched well with previous satellite studies by Weimer [1995] and Rich and Hairston [1994], but not well with previous statistical studies based on magnetometer measurements.

With these statistical patterns derived by SuperDARN measurements, a new tool was realized for the creation of a complete, global convection pattern based on radar measurements covering a significant portion (but not all) of the high latitude ionosphere. In this method, electric fields in data-sparse regions are constrained by the statistical patterns. The technique, derived by Ruohoniemi and Baker [1998] and validated by Shepherd and Ruohoniemi [2000], is discussed previously in this chapter and produced the electric fields used in this global high-latitude case study (illustrated in Figure 3.2).

2.7. Previous Ionospheric Simulations Using Model E-fields

The developers of the Time-Dependent Ionospheric Model at Utah State University have accomplished many validations of the model by running simulations using various inputs and comparing the results to both satellite measurements and to our physical understanding of the magnetosphere-ionosphere-thermosphere system. A comprehensive study was also accomplished by Groves [2002] using a side-by-side comparison of results using several inputs, and a density structure parameterization (DSP) technique was developed which deduces the fine scale density structures from an analysis of just a few input parameters.

The earliest studies accomplished at USU (discussed in section 2.4) helped to improve the state-of-the-art in ionospheric modeling through the incremental development of the TDIM. Further, more recent studies have proven the model's validity, and have also demonstrated the weaknesses and strengths of a variety of model input data. Sojka et al. [1998] simulated the magnetic cloud passage of January 14, 1988. This specific event day was chosen due to its remarkably steady or slowly changing IMF vectors throughout the magnetic cloud's passage. This steadiness should allow the ionosphere to develop characteristic plasma flow patterns that could be directly related to the corresponding IMF pattern. As Freeman et al. [1993] explain, while the summer (southern) hemisphere did routinely display these characteristic convection patterns, the winter (northern) hemisphere's response during this event could not be so confidently characterized. Therefore, simulations run for this event focused on southern hemisphere data. In their findings, Sojka et al. [1998] noted significant differences between simulation results derived from statistical electric fields and auroral precipitation and

results derived from the NRL MHD self-consistent inputs. The statistical model run did not agree well with DMSP density measurements. Sojka et. al. [1998] attributes this to several factors. First, the statistical auroral precipitation model used was based only on Kp index and not IMF orientation. Additionally, as we noted in section 2.4, the statistical convection pattern is based on averages taken under Kp 3+ to 4- conditions, then is scaled by changes in calculated 3-hourly Kp. This method was shown to be inadequate to describe a storm of this magnitude (Kp increased to over 6), as the satellite-measured cross polar cap potential drop (over 200kV) was far larger than the statistical model's value (near 130kV). The substantially weaker convection would fail to increase ion temperatures to their proper value, thus limiting the resulting increase in recombination rates. This would lead to higher-than-expected plasma density in the F-layer. The MHD-derived results were shown to match well with in-situ measurements, even though the convection electric field is somewhat overestimated in this model. A storm time well-defined tongue of ionization (TOI) is present with approximately the correct placement and intensity, and a polar hole, or the decrease in density due to enhanced storm-time convection, is accurately represented. The only major difference between in-situ data and MHD results is that a storm-enhanced density (SED) feature described by Foster [1993] is observed by the satellite in the lower mid-latitude afternoon sector and is not well represented in the TDIM-MHD simulation.

Groves [2002] in his dissertation extensively compared the TDIM simulation results by again using electric fields and auroral precipitation from the statistical models and the MHD model, but also added a simulation using data derived from the Assimilative Mapping of Ionospheric Electrodynamics (AMIE) procedure. This research

again covered the magnetic cloud passage of January 14, 1988 for consistency with the earlier Sojka et al. [1998] research. Since the AMIE input also provides self-consistent electric fields and auroral precipitation, improved results were again expected as compared to the statistical run. Groves verified the validity of the TDIM in modeling high latitude plasma processes by showing the general similarity and believability of the results using all three inputs. While agreement with DMSP in-situ data was again generally better by using AMIE inputs than by using statistical inputs, features such as the TOI and polar hole are successfully created by each of the three models. Placement and intensity vary with each, and both the MHD run and the AMIE run yield a better positioned TOI during storm-time. All input models are shown to yield similar results during quiet geomagnetic times while the IMF is northward. A complete discussion of TOIs and polar holes is provided in section 3.4.2.

III. Methodology

In this research, we will attempt to compare and contrast the results from the previous TDIM simulation studies to the TDIM results using a Super Dual Auroral Radar Network (SuperDARN) real-time radar E-field data. A complete comparison of density results will also be made to DMSP in-situ data available on the study day. Early in this research, our desire was to use the same magnetic cloud event as did the previous simulation studies. However, because SuperDARN radar datasets do not exist for the previously studied 14 January 1988 storm, a new event of interest was selected. Discussions with Dr. J.M. Ruohoniemi [private discussion, 2003] from the Johns Hopkins University (JHU) Applied Physics Laboratory (APL) led to our interest in the magnetic event of 23 February 2000. While perfect consistency with the prior research is lost by our change in case study day, we still attempt to generalize across the events by comparing the development of specific density structures in both events stemming from the time-development of certain IMF conditions with a specified solar terminator location. The benefit of the magnetic event chosen in this research will be discussed in section 3.1, as well as the known characteristics of the ionosphere on this study day. The method used to mesh available SuperDARN data into a format that TDIM can read highlights the discussion in section 3.2. Difficulties with this interface and our solutions to these difficulties will be discussed. TDIM runtime options used in our simulation is the topic of section 3.3. Here we will also bring to light some issues concerning the uncoupled nature of the convection and auroral inputs to the TDIM. Finally, we will discuss the limitations of DMSP in-situ data and model output manipulation in section

3.4, to include a summary of the density structures we will attempt to use in our comparisons.

3.1. Characterization of the Simulation Study Day

As background, the previously simulated 14 January 1988 case study was valuable for several reasons. As Knipp et al. [1993] conclude, there are three essential characteristics about that storm's observed solar wind and magnetospheric fluctuations that make it a good candidate for study: large amplitude peaks, smooth features, and long time constants. These three features allow one to ignore small changes in space and time scales while expecting large classical ionospheric responses to the magnetospheric stimuli. For these reasons, Sojka et al. [1998] and Groves [2002] both used this event for their TDIM simulations. Our 23 February 2000 case study day is unique in a couple of ways. First, it does not qualify as a "magnetic storm", as the southward component of the IMF is relatively small and fleeting during the time of interest, and the Dst ring current index is unaffected. Second, while long time constants are still present, it is the unusually strong and persistent positive z and positive y components of the IMF that may lead to interesting and unique plasma convection patterns. These patterns will be illustrated and discussed later in this section, while the resulting plasma density structures will be discussed in the results chapter. First, we must start with the basics of the study day.

3.1.1. Solar Cycle, IMF Vector Data, and Geomagnetic Index.

February 23, 2000 was nearly at the peak of solar cycle 23. According to data available from the SEC in Boulder, Colorado, the 10.7 cm radio flux was 185 on the study day. The peak monthly F10.7 in the cycle occurred in December, 2001, however a

local maximum occurred in March of 2000, peaking just above 200. While the sun was rather active, the period was geomagnetically quiet. The weekly discussion issued by the SEC for the week of 21-27 February 2000 announced that a magnetic cloud from an earlier CME struck the magnetosphere on 21 February, then quiet conditions prevailed until a coronal hole moved into favorable position beginning late on 23 February and into 24 February. This left our study day with moderate solar wind plasma densities of $10\text{-}40\text{ cm}^{-3}$ and a moderate solar wind speed of $400\text{-}500\text{ km/sec}$. The Advanced Composition Explorer (ACE) satellite, located at the L1 libration point 1.5 million kilometers from Earth, consistently measured these solar wind parameters, as well as the IMF vector structure through the period. Figure 3.1 shows the IMF (in GSM coordinates) as measured by ACE as well as the associated planetary geomagnetic index (K_p) existing on Earth. It is assumed here that the IMF measured at the L1 point traveled to Earth's magnetosphere without significant changes in structure. This assumption is often made since the GSM x-component of the solar wind speed is significantly larger than its associated y- and z-components. Note that we used the solar wind speed to delay the arrival of the IMF measured at ACE by 54 minutes so that comparisons can be made between the IMF components measured at ACE and the K_p measured here on Earth.

3.1.2. Simulation Runtime Selection Criteria.

The four numbered markers at the top of Figure 3.1 represent the times that were selected as runtimes for the TDIM ionospheric simulation. There were two general considerations made in the selection process. The first was the positioning and persistence of the IMF vector, and the second was the coinciding time of the DMSP satellite pass. All four of the runtimes were chosen due to different interesting

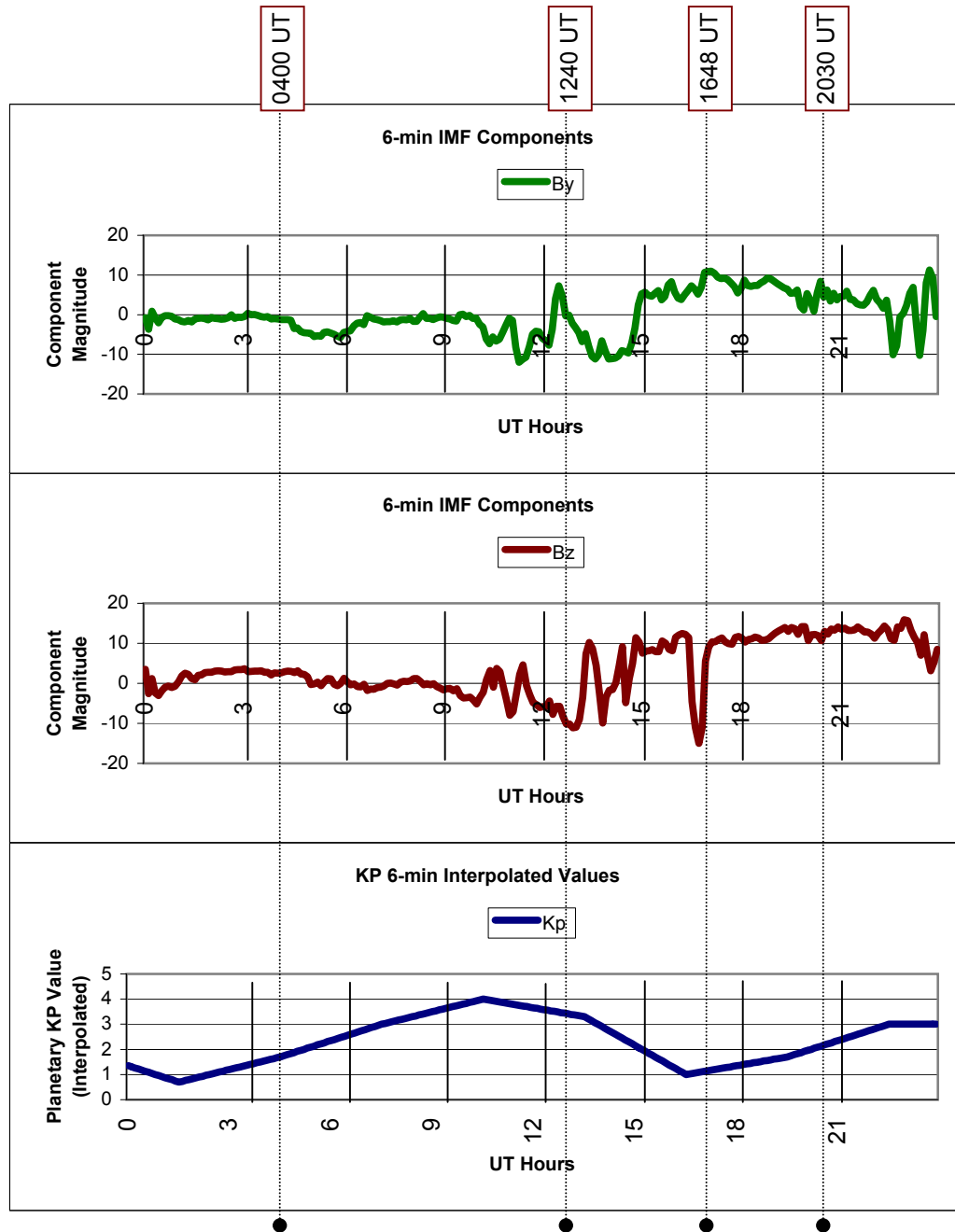


Figure 3.1. Timeline plots of solar wind IMF components with the associated geomagnetic index (K_p) on 23 February 2000. IMF data is taken from 4-min resolution ACE level-2 data (thanks to ACE MAG instrument team, ACE Science Center) while K_p is interpolated from the standard 3-hour planetary index (thanks to NGDC).

characteristics of the IMF at the time considered. Since the SuperDARN-observed data contained few data-sparse areas on this study day, we can assert that statistical data did not shape the convection pattern, as discussed in section 2.5. It should also be noted that while the convection patterns at each runtime are displayed on Figure 3.2, unique convection patterns for each 2-min interval have been supplied for the TDIM 24-hour simulations. Because of this, the simulation results discussed in the next chapter are a result of not only the convection pattern at the selected runtime, but of the continually changing convection pattern throughout the previous 24-hour period.

Runtime 1 at 0400 Universal Time (UT) was selected due to the very small negative B_y component and the small but unwavering northward (positive) B_z component measured over the three hour period between 0100 UT and 0400 UT. We expect this period to be long enough to allow the convection pattern to obtain a “characteristic” quiet time pattern for these IMF conditions. In addition, since geomagnetic conditions were reported to be quiet for 22 February as well, it is hoped any storm-time ionospheric density structures that developed previously had dissipated in the ionosphere by this time. The upper convection maps of Figure 3.2 display both the SuperDARN pattern (left) and the Heppner and Maynard [1987] statistical equipotential pattern (right) for 0400 UT. It should be noted that while the SuperDARN plot on the left does not contain smooth, circular contours representing the co-rotation electric field outside the convection pattern, the TDIM automatically adds co-rotation to this pattern to ensure consistency with the statistical pattern on the right. According to the SuperDARN measurements, the entire convection pattern is contained north of 70° , and the cross polar cap potential drop is only 27 kV. The dusk convection cell is dominant (the dawn cell

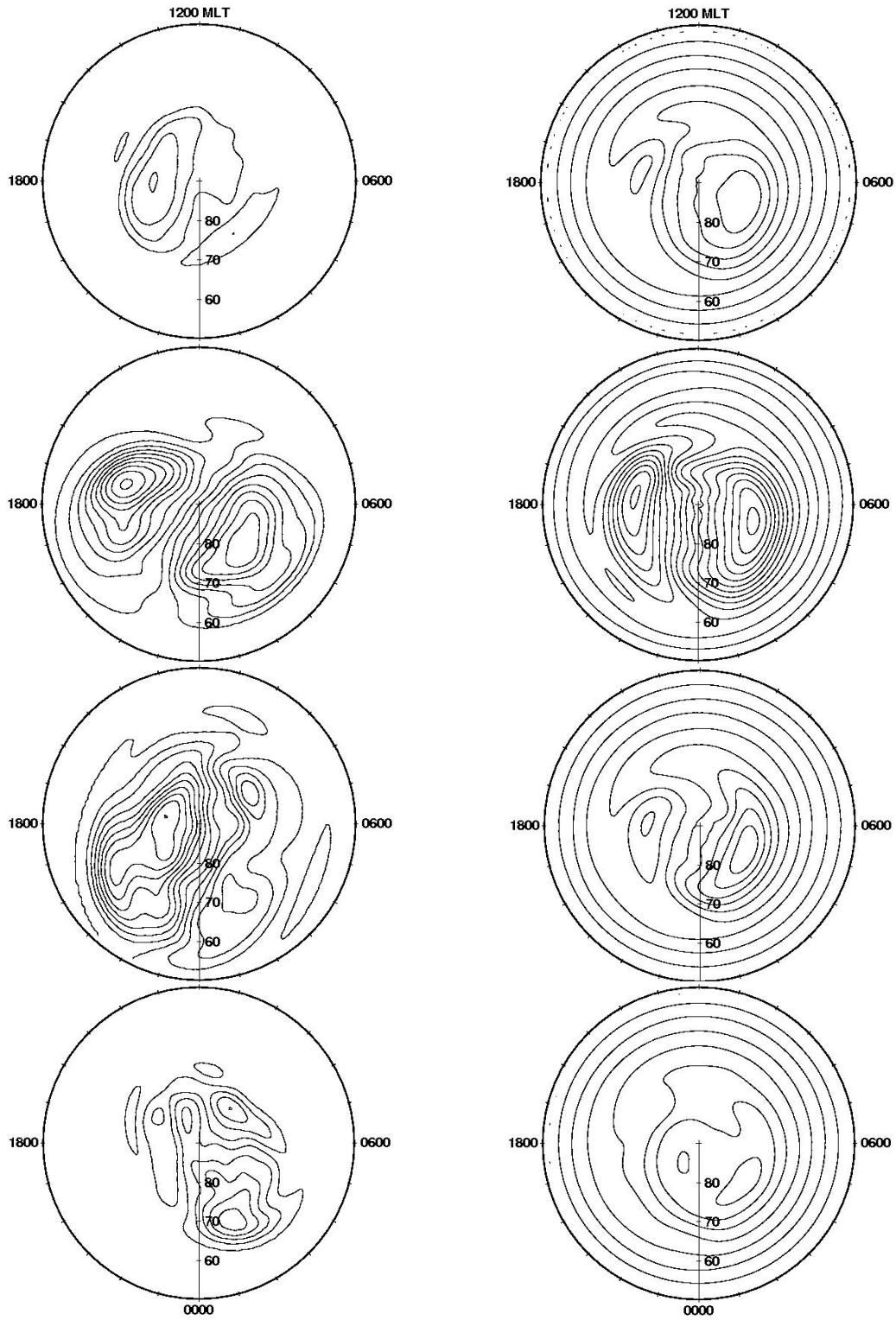


Figure 3.2. Convection inputs using SuperDARN measurements (left) and statistical patterns (right). The universal times are 0400 (top), 1240 (row 2), 1648 (row 3), and 2030 (bottom). Magnetic local times are labeled around the perimeter of the dials. The contour spacing is 5 kilovolts.

dominates the statistical pattern) and dusk to dawn plasma motion exists across the noon meridian (dawn to dusk for the statistical pattern). The SuperDARN pattern matches very closely with the findings of Bristow et al. [1998] during a period with nearly identical IMF conditions.

Runtime 2 at 1240 UT was selected considering both the IMF and DMSP satellite high-latitude pass times. The period 1130 UT to 1320 UT was characterized by a consistently southward Bz component (5-10 nT) and a small (<5 nT) and negative By component, except for a brief 20 minute period of a small positive By. Ideally, we would select a time at the end of a period where both Bz and By are consistently of the same polarity; however, the in-situ data availability limits us here, as the only DMSP pass available in the southward Bz period crosses the north polar cap at around 1230. For this reason, we have selected 1240 UT as a reasonable approximation that gives us both a significant southward Bz component, as well as a time where in-situ data are available to verify our simulation results. The second row of charts in Figure 3.2 illustrates the SuperDARN and statistical versions of the convection pattern resulting from these IMF conditions at 1240 UT. Both patterns are similar, but the SuperDARN pattern has a stronger dusk cell, whereas the statistical pattern maintains a stronger dawn cell. In addition, the SuperDARN pattern shows plasma convecting across the noon-midnight meridian in a dawn to dusk direction, whereas the statistical pattern contains plasma convection directly anti-sunward along the noon-midnight meridian. An important item of note is that at 1240, the By component of the IMF has just (in the previous two minutes) turned slightly negative from a previous 18 minute period of 5-10 nT positive By. Thus, while the statistical pattern has instantaneously been selected through binning

criteria to be convection pattern model A (see Figure 2.6) with the shift of the IMF B_y component to negative, the SuperDARN convection pattern still has the characteristics of a positive B_y pattern similar to model BC (Figure 2.4). From the work of Ruohoniemi et al. [2002], we would expect the observed convection pattern to show the instantaneous response of the ionosphere to the specified change in the IMF. However, we note that the propagation of the IMF from its observation at the ACE satellite to its incidence on the ionosphere was approximated. While a 54 minute travel time was used during the entire study day calculated from the 24-hour average speed of the solar wind, the speed actually changed during the period, from a minimum of 400 km/sec at 0000 UT to a maximum of 500 km/sec at 2400 UT. This could lead to time errors of a few minutes when the actual solar wind speed is significantly different from the average speed. An error of just two minutes would lead to a change in the statistical convection pattern during such periods when an IMF component changes its sign.

Runtime 3 at 1648 UT was selected because of the sharp, relatively strong (~ 15 nT) B_z southward turning of the IMF in the 20 minute period preceding this time. Our effort here is to characterize the time necessary for the convection pattern, and in turn the ionosphere, to react to such an abrupt and significant change in polarity of the IMF. Conceptually, a shift of the IMF to B_z negative should create rapid effects in the convection pattern because Earth's dipole field is immediately open to the IMF. Ruohoniemi et al. [2002] showed that the convection pattern changed globally and simultaneously on a time scale of a few minutes. The third row of plots in Figure 3.2 shows a significant difference in cross-polar cap potential drop between the two convection patterns. The observed SuperDARN pattern has a dusk-side potential

minimum of -45 kV, and the general pattern is as one would expect of a strong 20 minute period of southward B_z (10-15 nT) and positive B_y (5-10 nT). Note the small-scale structure observed in the split dawn cell. The statistical pattern contains a dusk-side potential minimum of only -26 kV and a standard, smoothed two cell pattern with the centers of the cells shifted a couple of hours earlier than the dusk-dawn line (as expected with a positive B_y). We note the relatively weak statistical pattern even with southward B_z , and estimate that this is due to the very small planetary K_p index in the period of just over 1. This is a clear weakness of statistical convection patterns that depend upon K_p . Even though a strong southward B_z component exists, ionospheric substorming was not sufficient to cause a significant change in the K_p index. We attempt to verify this rapid response in the ionosphere by comparing ionospheric density simulation results based on this pattern with DMSP density measurements. Results will be shown in the next chapter.

Finally, runtime 4 at 2030 was selected due to the uncommonly strong and steady B_z north and steady B_y positive IMF configuration of the period 1700 UT to 2200 UT. As the bottom row of plots in Figure 3.2 shows, both convection models show a sunward plasma flow in the sunward side of the polar cap during this time. In fact, the SuperDARN observations resemble the Heppner and Maynard [1987] rotationally twisted BC model (see Figure 2.7). We hope through our TDIM simulation run to discover an atypical density structure in the ionosphere due to this reversed convection pattern. Discussions in this paper will focus on how the electric field inputs affect the simulation density results for these four marked times.

3.2. Interface between SuperDARN Data and the TDIM Model

One of the major challenges facing near-Earth modelers is the consolidation and standardization of real-time data measurements of many ionospheric and magnetospheric parameters. Our research brethren in the terrestrial weather field have a standardized medium for observation transmission. Members of the World Meteorological Organization (WMO) around the world encode surface and upper-air observations in a standardized code for everyone to share. For this reason, modelers can ingest data from a variety of locations, and use it in common, global specification and forecast models. In near-Earth space physics, however, data are measured, both directly and indirectly, under different conditions, using different platforms, and set in different coordinate systems. The resolution of the data are often different, both spatially and temporally. Indirect measurements are often taken of magnetospheric current systems, and then results are applied to electric field convection patterns. Current state-of-the-art researchers at Utah State University's Center for Atmospheric and Space Studies (CASS) are actively finding ways to coherently combine measurements from diverse observational platforms. The challenges of reformatting data for model assimilation have been a major hurdle in this research as well, and this section will discuss how we have dealt with these challenges.

According to Ruohoniemi and Baker [1998], SuperDARN data are collected and presented in an Altitude-Adjusted Corrected Geomagnetic (AACGM) coordinate system. In this system described by Baker and Wing [1989], the magnetic coordinates presented are akin to standard corrected geomagnetic coordinates but are adjusted according to the altitude of interest. Also, in an effort to standardize bin size between the common coverage areas of pairs of radars, a larger number of bins is developed near the low-

latitude limit of the coverage area than in the very high latitudes. This allows each bin, or grid “square”, to contain an approximately equal physical area, with each box having dimensions of approximately 111 km (1° latitude) x 111 km (variable longitude degrees, depending on the latitude). The data are presented in files by increasing latitudes, with the lowest latitude first. Within each latitude, the data are presented in order of increasing AACGM longitudes, starting at 0°. The data array has more elements at lower latitudes (due to a larger number of bins) than at higher latitudes. Ruohoniemi and Baker [1998] state that this irregular construction was chosen for two main reasons. First, it is preferable to average velocity measurements than to use individual velocity measurements. This is because the near-radar regions would be oversampled as compared to the far-radar regions, and results would be skewed by the large number of individual measurements sampled close to the radars. Second, it was considered that other types of velocity measurements may need to be compared to the radar-sampled measurements. As ground measurements tend to be taken in a similar spatially-consistent manner, data can be easily compared. Figure 3.3 provides an example of line-of-sight velocity measurements overlain on this grid.

As with any multi-piece network, not all members of the network are always functioning. There are also times when some of the radars are being used for independent studies, meaning data from that radar may not be sampled with the same temporal or spatial resolution, and are therefore not included in this study. In addition, one of the radars may not have received enough backscattered energy from velocity irregularities to resolve the two-dimensional plasma velocity from measurements received by another radar. Due to many of these limitations at different times in the

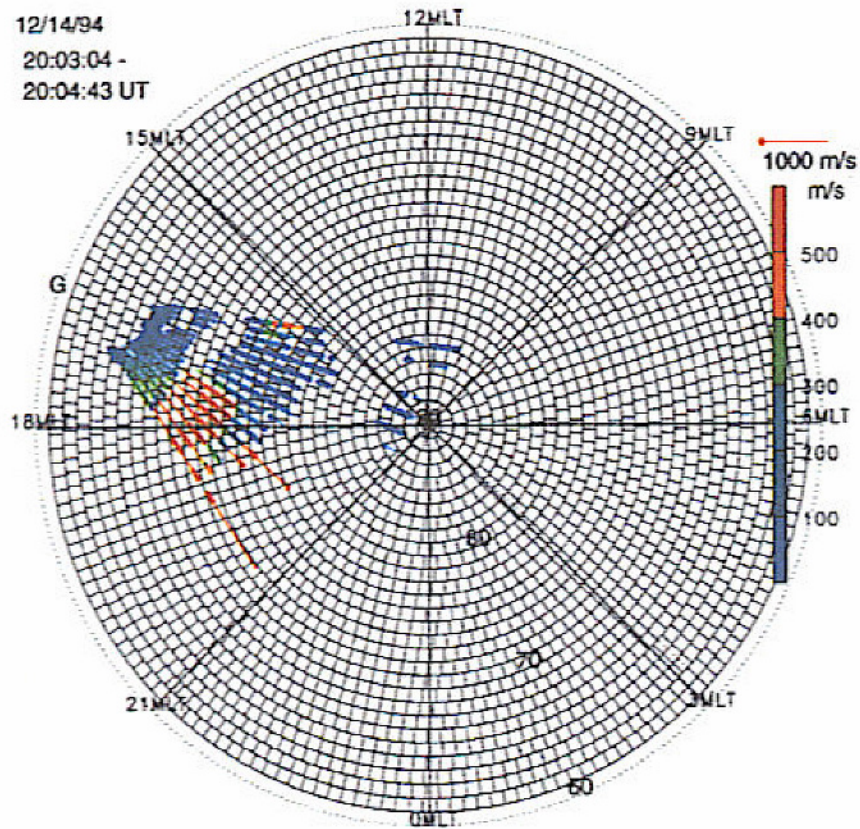


Figure 3.3. Plot of the grid for spatial averaging of the line-of-sight velocity data. A sample of velocity data from the Goose Bay radar is shown. The outer dashed circle corresponds to a magnetic latitude of 60° , and 3-hour magnetic local time (MLT) meridians are added. The position of the radar in magnetic longitude is indicated on the 60° contour by the letter G. The velocity data are scaled to the length of each arrow and are also color-coded by magnitude [Ruohoniemi and Baker, 1998].

study day, some periods may contain only data sampled by six or seven of the nine radars. Whatever the case, since the lowest latitude present in the SuperDARN data file depends on the lowest latitude of velocity measurements resolved, the number of latitudes contained in each 2-min period is variable.

The result of all these irregularities in array size led to many complexities in the data interface with TDIM. The resulting SuperDARN grid is not at all consistent with the grid used for input into the TDIM. Additionally, the coordinate system used by TDIM is an Earth-centered dipole system. The difference between this system and the AACGM system can be significant, especially near the pole. Second, the TDIM uses a square 101x101 array to map parameters over all latitudes. We will hereafter refer to this grid as a “J-K grid”. The dipole pole of this J-K grid is located at grid location J=51 and K=51, or at the exact center of the grid. While the grid box sizes cover a constant geographic area over the entire map, just as in the SuperDARN case, the orientation of the boxes is different. Figure 3.4 illustrates this gridding, although the figure reduces the mesh from 101x101 to 17x17 for ease of viewing.

In order to place the correct electric potential value from the raw SuperDARN data files into the correct J-K bin for use by TDIM, several processes needed to be accomplished to the raw SuperDARN data. First, since the size of the bins between the two formats was different, interpolation of the raw data needed to be accomplished so that each of the 101x101 J-K bins could contain data. A two-dimensional linear interpolation was used here for simplicity, and each interpolation was accomplished separately (longitude, then latitude) due to the different number of bins at different latitudes. The size of the final interpolated array was estimated, and then increased to

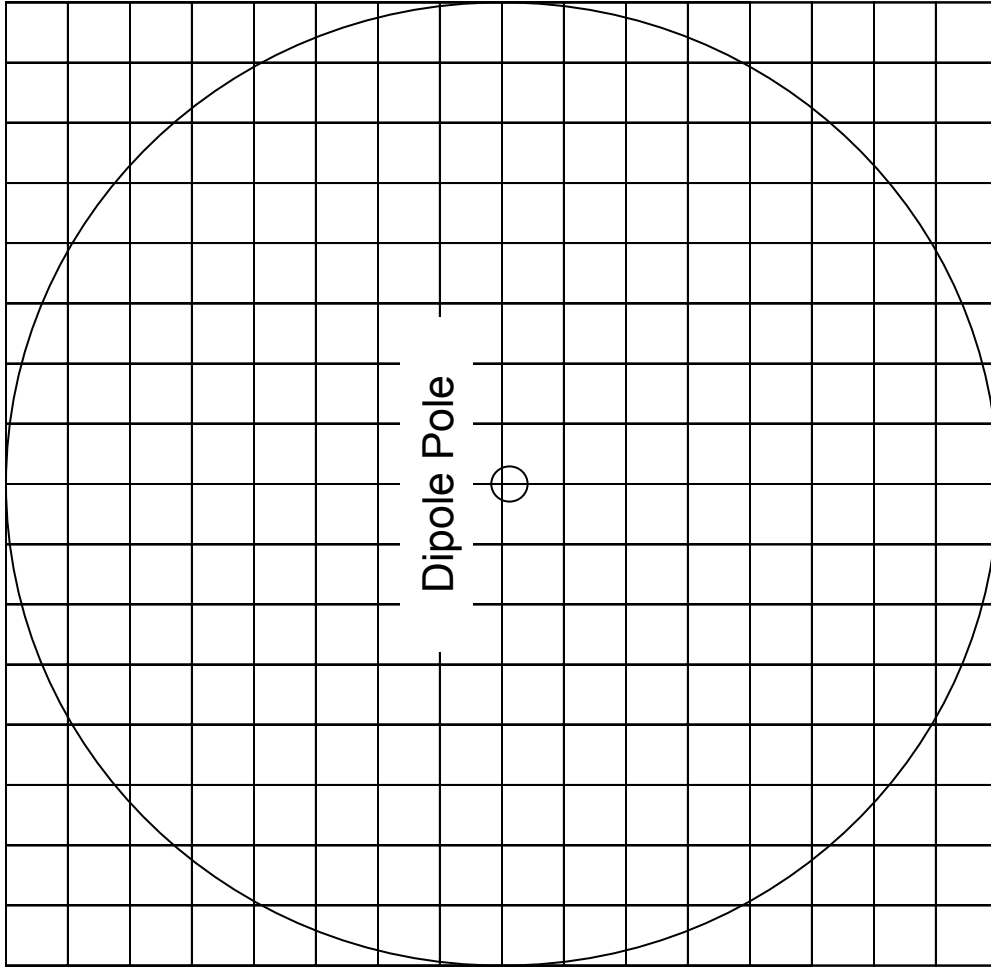


Figure 3.4. An example of a square grid such as the one used in TDIM. The large circle represents the 50 deg invariant latitude line. Grids centered outside this circle are located at lower latitudes. Note that the TDIM runs in this study use a 101x101 array size rather than the 16x16 shown here. This was displayed for the sake of simplicity.

remove any chance of holes where data from the interpolation was insufficient to fill every J-K bin. A longitude interpolation was completed first, and the electric potential data was placed in bins equally spaced from 0° to 360° at each latitude. Once this was accomplished, each latitude “row” contained an equal number of bins, thus an interpolation across latitudes could then be completed. Just as with the longitude interpolation, electric potential data were placed in equally spaced bins, this time from 50° to 90° latitude. A value of the potential at exactly 90° was ascertained by averaging all of the potentials from the highest latitude less than 90° (normally 89.8°). Due to file size limitations, the size of the interpolated SuperDARN data array was limited to 600×200 . Now that the data were in a regular, interpolated array, we could then smartly fit the data into the J-K grid for use by TDIM. The position of each J-K bin (initially provided in dipole coordinates) was converted to AACGM coordinates via software from the Applied Physics Laboratory at Johns Hopkins University (many thanks to Dr. Mike Ruohoniemi). We must note that an altitude location of each bin was not specified, since the TDIM J-K coordinate system is not altitude-adjusted. We then found the interpolated potential value from the interpolated array which was located closest to the latitude/longitude position of each empty J-K bin. This process we call “smart selection”. In selecting this closest position, the inherent error involved in placing the data into the proper J-K bin was calculated as half of the size of each newly interpolated grid square. To test our smart selection and interpolation method (together, the “smart-interp” method), we plotted a convection map using the 600×200 interpolation routine and compared it to a map created without using the method. Results are displayed in Figure 3.5. Since we had initially used SuperDARN data without using the smart-interp method,

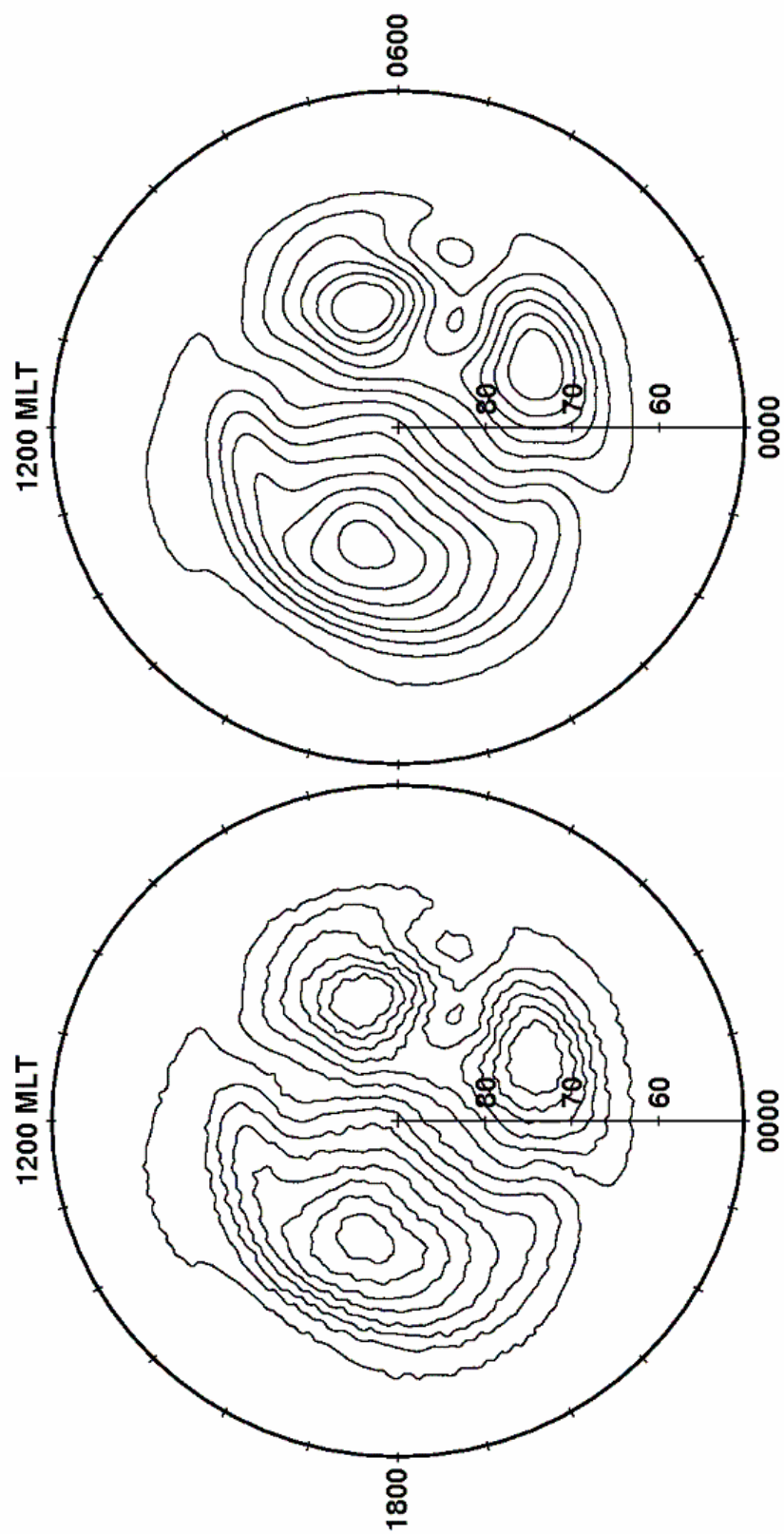


Figure 3.5. Pre-interpolated SuperDARN convection pattern (left) vs. post-interpolated pattern (right).

our initial TDIM simulation results were skewed by the artificial turbulence in the convection pattern shown on the left plot of Figure 3.5. Specifically, every time plasma near the low-latitude boundary of the convection pattern is moved poleward (due to the turbulence), it is also raised upward via vertical $\mathbf{E} \times \mathbf{B}$ drift. Each time plasma in this region moved anti-poleward, it is lowered via the same physical argument. Artificial upward (downward) vertical motions cause parcels of plasma to maintain higher (lower) equilibrium densities due to a decrease (increase) in recombination rates at their new altitude. The TDIM simulation result from our initial use of a turbulent convection pattern is shown in Figure 3.6. The first plot shows vertical drift caused by a combination of vertical $\mathbf{E} \times \mathbf{B}$ drift and neutral wind-induced field-aligned air drag. The speckles coincide with the poleward motion created by artificial turbulence in the convection pattern leading to vertical $\mathbf{E} \times \mathbf{B}$ drift. The second plot shows the resulting erroneous variation in densities in the top-side ionosphere. The splotchy appearance in the density plots reduced our ability to match density features in the simulation results with in-situ measurements, which led to our development of the smart-interp method. The third plot shows top-side ionospheric density results using our resolved smart-interp convection pattern. While we will discuss features displayed on these density maps in the results chapter, we were compelled to provide a small sample here to illustrate the need for an interpolation method.

3.3 Running the TDIM: Difficulties and Adaptations

Once the SuperDARN data are prepared for input into the TDIM, simulations could be prepared and executed. The TDIM itself is a very large, complex FORTRAN

Turbulence Effects

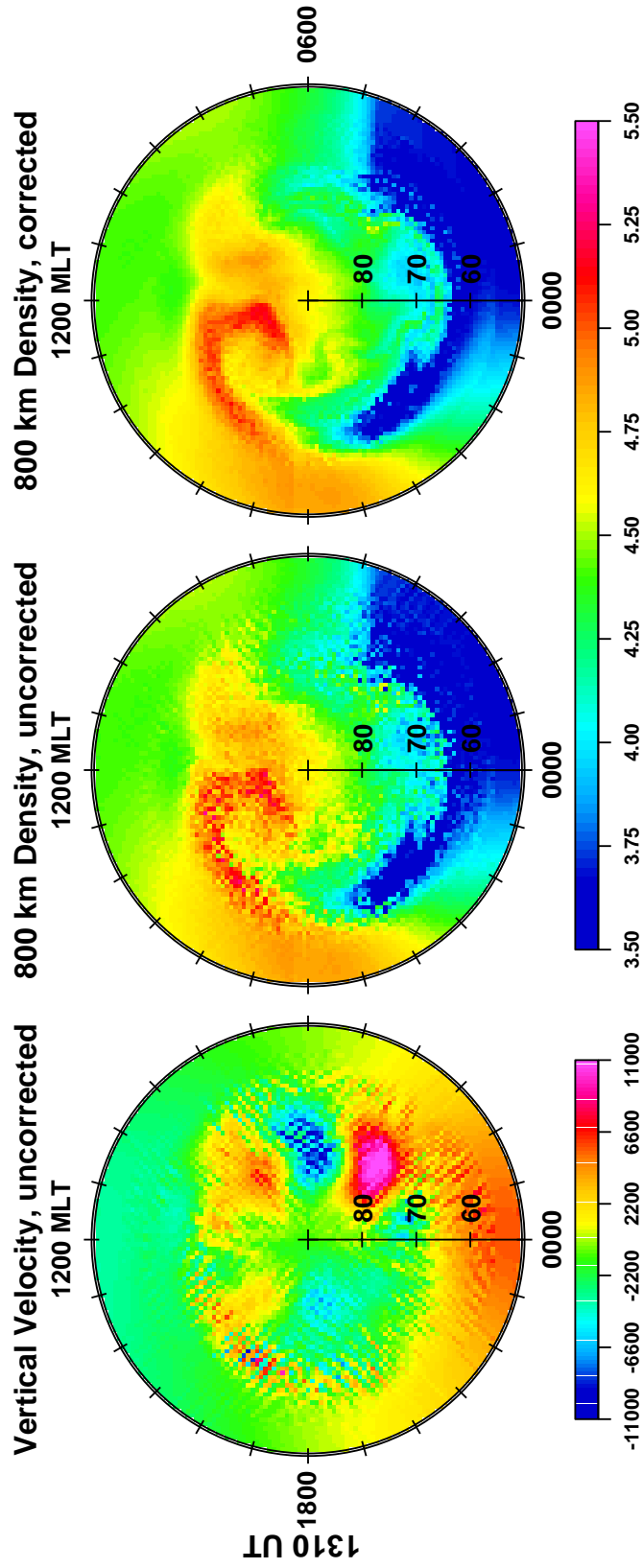


Figure 3.6. 1310 UT TDIM simulation results for the vertical speed (left, positive upward) and 800 km density using non-interpolated SuperDARN data (middle) and interpolated SuperDARN data (right). The maximum variability in vertical speeds can be found in areas away from the polar cap where artificial turbulence has been created. This variability leads to the spotty density results found in the middle plot.

program with an extensive library of subroutines. Simulations were prepared for execution by setting the model's on/off switches through a command file and by pointing the model to the proper input parameters to use with each run. For example, in order to decrease the extensive computational load, a setting was used that allowed TDIM to use only hourly SuperDARN-supplied convection patterns at the beginning of the 24-hour simulation period. TDIM then increased the cadence of the input SuperDARN pattern to the full two-minute resolution near the end of the period. For example, for the 1240 UT runtime, convection patterns were brought into TDIM at an hourly cadence from 1240 UT to 1840 UT on 22 February 2000. The cadence was gradually increased until the full two-minute resolution of input patterns was used between 0640 UT to 1240 UT on 23 February 2000. In addition, in order for the correct Hardy et al. [1987] auroral precipitation pattern to be used, a file containing the planetary Kp index was supplied. In order for the proper Heppner and Maynard [1987] convection pattern to be used (for the baseline statistical run), a file containing both the Kp and the time-delayed IMF By and Bz components was supplied. In this section, we will describe the challenges we faced to create reliable physical results as well as the artificial adaptations that were necessary to achieve these results.

As we have touched on throughout the paper, the SuperDARN convection electric fields used as inputs into TDIM are independent of the auroral precipitation pattern used by TDIM, which are taken from the Hardy et al. [1987] model. Sojka et al. [1998] and Groves [2002] all discuss the benefits of using coupled inputs in their studies using MHD and AMIE inputs to the TDIM. We also intend to display here evidence showing the effects of inputs that are not self-consistent.

It is understood that there are magnetospheric drivers responsible for a convection electric field pattern and auroral precipitation. Convection should coincide with the auroral precipitation in both coverage area and also in magnitude. Since our inputs for the TDIM-SuperDARN runs were independent of each other (observed E-fields vs. statistical precipitation), consistency was not guaranteed. The input models that were used in this research were decidedly inconsistent because of the incongruity between the Kp index, upon which the Hardy et al. model is based, and the real-time IMF incident upon the magnetosphere, which is the primary driver of the observed convection pattern. While short bursts of energy can be added to the ionosphere through brief episodes of reconnection in the magnetotail during IMF Bz southward conditions, the Kp index “blurs” a brief geomagnetic impulse across an entire three hour period. We showed in the last chapter how the slow response and the coarse nature of the planetary Kp index caused a significant underestimation of the equatorward extent of the statistical convection pattern (scaled by Kp) during one of these short bursts of IMF Bz south near 1648 UT. Here we can posit that a self-consistent auroral precipitation and convection electric field model would have displayed an immediate reaction in both parameters during short episodes of reconnection due to its self-consistent nature. We use Figure 3.7 as an illustration of our quandary. The first map shows the Hardy et al. flux in response to the geomagnetic conditions at 0400 UT, when the interpolated Kp was 1.53. Comparing with the observed convection pattern in Figure 3.2, the auroral oval is at latitudes completely removed from the convection. Indeed, the electron precipitation is occurring in a region of quiet, co-rotating plasma. The second map shows the other extreme which occurs at 1648 UT. Even though Bz is strongly southward and the

Effects from Uncoupled Models

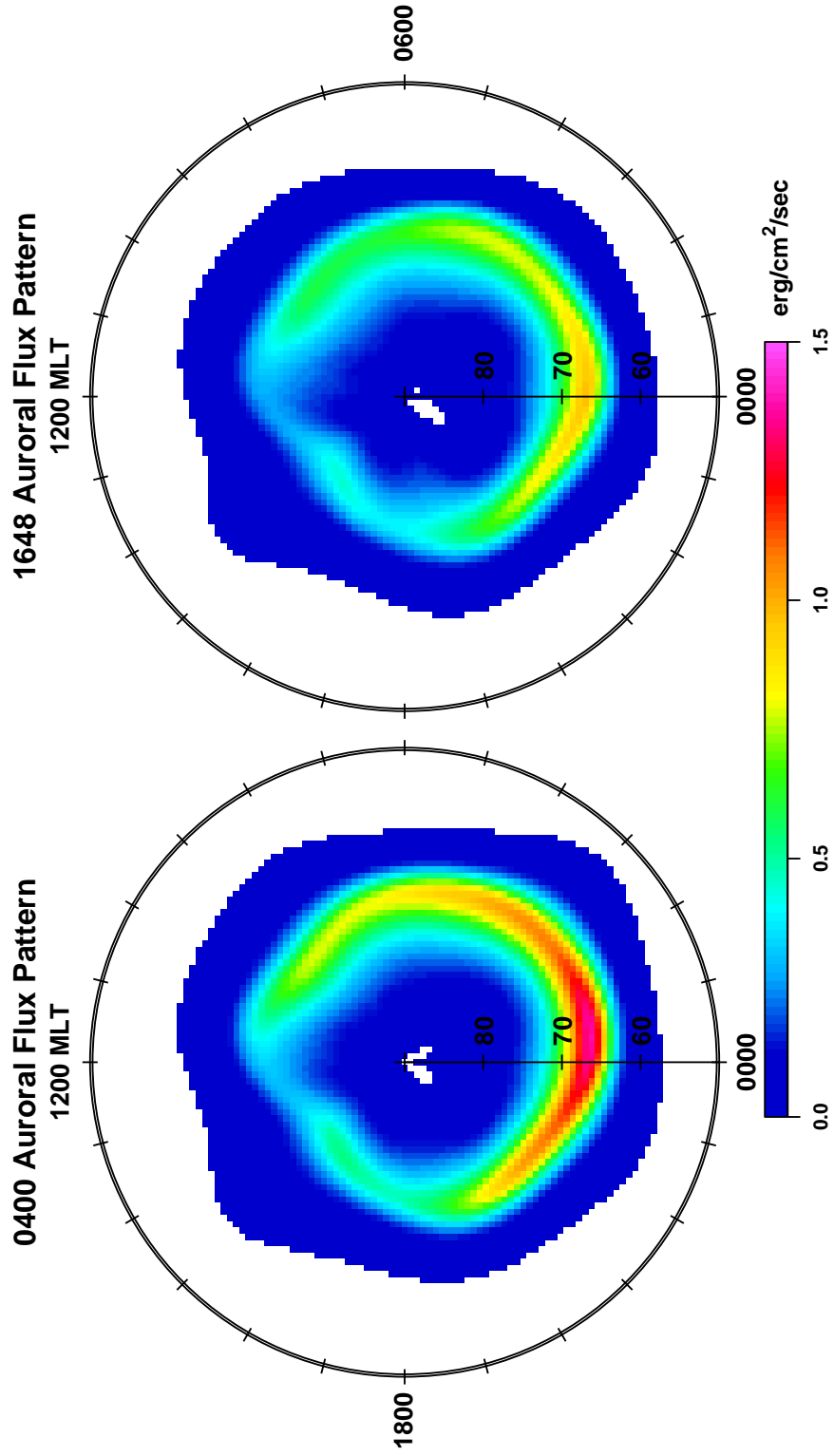


Figure 3.7. Statistical (Hardy et al., 1987) precipitating electron flux at 0400 UT (left) and 1648 UT (right). Dark blue areas outside the auroral zone signify noise level flux and can be ignored. Note that while the later period is more geomagnetically active than the earlier time due to a moderate southward IMF, an unresponsive Kp index has produced a smaller precipitating flux at this time.

observed convection pattern has expanded to nearly 55° latitude, the interpolated planetary Kp index of just over 1 has resulted in markedly underestimated electron precipitation. We can easily argue that reconnection stemming from a 20 minute Bz southward component of 15 nT should lead to an enhanced auroral energy input over this period, not a quiet-time electron precipitation pattern accompanying a Kp of 1.

While identifying erroneous plasma density structures in a simulation run due to uncoupled inputs is extremely difficult given the time-dependent nature of the ionosphere's structural development, we believe we found one such problematic structure in our preliminary results. The first plot in Figure 3.8 is a map of top-side plasma density at 1310 UT using SuperDARN convection and standard Hardy precipitation. During this time, the convection pattern input to TDIM was very similar to the pattern shown in Figure 3.2 for 1240 UT. We note the high-density ring of plasma at approximately 65° on the midnight side of the dial plot. The second plot shows neutral wind flow where negative quantities represent flow toward the pole. Unsurprisingly, the neutral winds flow from day to night across the pole. We submit that the “smile” of higher densities stems from upward vertical motion of plasma due to neutral wind-induced field-aligned air drag. Normally, with coupled input parameters, a relatively strong channel of horizontal drift should exist at nearly the same nightside latitude as the auroral electron flux. This channel of high speed plasma would increase ion temperatures and therefore increase recombination rates. As Groves [2002] explains, the enhanced density depletion from the high speed channel in the outer part of the convection pattern will be the dominant parameter over neutral wind-induced field-aligned air drag, which has a much longer time constant. Therefore, the “smile” would not form. However, at this runtime

Enhanced Topside Auroral Densities

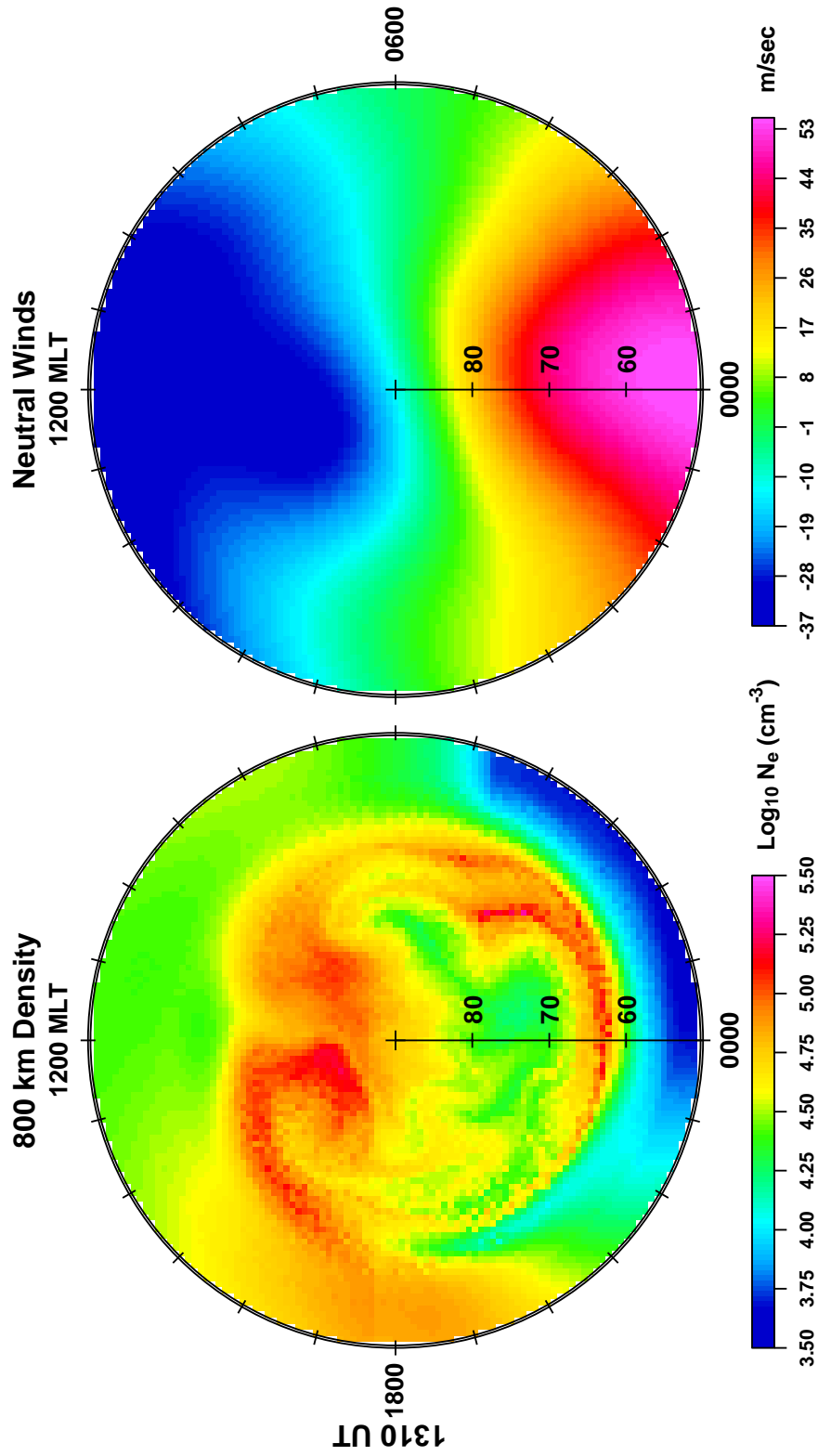


Figure 3.8. 1310 UT TDIM simulation results for 800 km density (left) and statistical (HWM-90) neutral wind speed (right). The combination of upward neutral wind-induced field-aligned air drag and overestimated precipitating flux into latitudes outside the prevailing convection pattern over long periods have resulted in enhanced topside densities in the 65° latitude antisunward regions.

of our simulation (and many others as well), the auroral electron flux occurs outside the convection pattern. In fact, due to slightly elevated Kp values of near 4 and a relatively contracted convection pattern (see Figure 3.2), we can assert that the statistical auroral electron precipitation pattern stays outside the convection pattern for several hours. This allows the dominant transport process in this region to remain upward air drag for a lengthy period. This, in turn, leads to the artificial density enhancement at 800 km, as we will discuss shortly. We note here that the length of the quiet period necessary for such a conceived density structure is not known from our literature search.

Arguments for the artificiality of the “smile” of high densities in the nightside auroral zone are difficult to verify through in-situ measurements. None of the DMSP density-sensing satellites make passes over the nightside ionosphere at these latitudes. However, we have attempted to show the validity of our argument by using the available on/off switches inherent to the TDIM. One such switch allows the modeler to “turn off” the neutral winds moving across the pole. Setting neutral winds to zero allows us to test the mechanism behind the enhanced “smile” of plasma. Without the neutral wind causing the upward plasma motion at nightside mid-high latitudes, enhanced plasma densities in the E-region auroral zone or simply the higher densities of the F2 peak should never have an effect on top-side plasma densities. Another such switch allows the modeler to set the auroral electron flux equal to zero. This will allow us to test the source of the high density plasma: the E region through an extended period of upward air drag or simply upward drag of the higher density plasma near the F2 peak. Figure 3.9 shows the results of these simulations. The first plot was created by TDIM with neutral wind set to zero, while the second resulted from a simulation with zero precipitating electron flux.

Possible Fixes for the Erroneous Densities

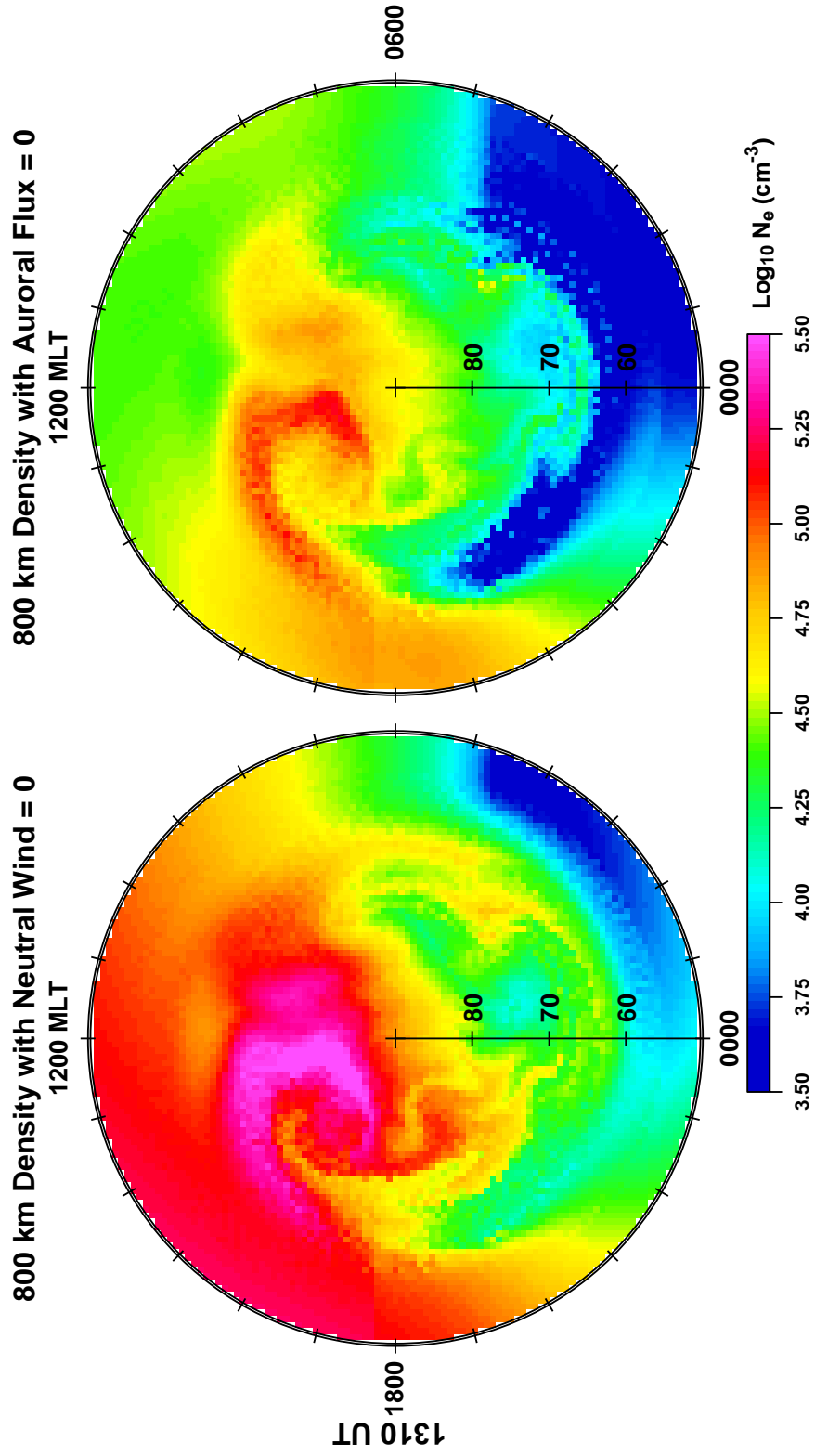


Figure 3.9. 1310 UT TDIM simulation results for 800 km density with neutral wind set to zero (left) and auroral precipitation set to zero (right). While both model settings removed the non-physical ring of enhanced topside density in the auroral zone, the former added a unique artificiality: increased dayside densities due to the removal of downward neutral wind-induced field-aligned air drag.

It is clear from a comparison between these dial plots and the density plot in Figure 3.8 that both special cases remove the enhanced density feature in the nightside auroral zone. The charts also illustrate how little an effect that “turning off” the aurora has in the high-latitude topside ionosphere (naturally this would *not* be the case in the high latitude E region), while it is obvious that neutral wind-produced effects are pronounced in many MLT regions in the 50°-70° range. Due to our findings, we believe uncoupled magnetospheric input parameters are the cause of the nightside plasma density structure discussed here, and that setting auroral flux to zero will allow us to better study the effects of different convection patterns on high latitude topside density structure without causing undesirable effects on our topside ionospheric density results.

3.4. Plotting Model Results

Once the output file has been created for each TDIM run, many plots can be generated through the model’s available plotting routines. Local parameters can be mapped at any of 37 altitudes in a range from the E layer up through the top-side of the ionosphere (F2 peak up to 800 km). We will focus on parameters plotted at this upper limit, as DMSP in-situ data corresponds to the satellites’ high-latitude orbital altitude of approximately 830 km. This section of methodology will first focus on the availability of and limitations on this DMSP in-situ data. We will then discuss the density structures for which we will search in order to make appropriate comparisons with this in-situ data.

3.4.1. DMSP Satellite Availability and Limitations.

According to the National Geophysical Data Center (NGDC) website, the Air Force Space and Missile Systems Center (SMC) Defense Meteorological Satellite

Program (DMSP) designs, builds, launches, and maintains satellites monitoring the earth's meteorological, oceanographic, and solar-terrestrial physics environments. Currently, the operational satellites are named F13, F14, and F15. F12 is still functional and is now considered in its extended lifetime. Each satellite maintains a 101 minute, sun-synchronous, highly inclined orbit near an altitude of 830-840 km above the earth's surface. One of the satellites, F13, maintains a nearly dusk-dawn (~1700-0500 MLT) orbit while the other three orbit from approximately late evening to late morning (~2130-0930 MLT). The sensor package which provides the plasma density readings we use in this research is the Special Sensors-Ions, Electrons, and Scintillation (SSIES) thermal plasma analysis package. Specifically, the Retarding Potential Analyzer (RPA) instrument provides ion density measurements, ion temperature, and fractional composition of the plasma in H^+ , He^+ , and O^+ every 4 seconds. Other instruments in the package include the Ion Drift Meter (IDM), which measures plasma drift velocity components V_x , V_y , and V_z relative to the satellite's motion and the Langmuir Probe, which measures electron density and temperature. All instruments in the package are held at the ambient plasma potential so that negative surface spacecraft charging due to photoionization of the metal in sunlight does not hinder the sensor's ability to gather electrons or improperly aid the sensor in gathering ions. The device that monitors the ambient plasma potential is called the SENPOT device.

One limitation which we faced in finding quality DMSP in-situ data was equipment outage on the spacecraft. The F14 satellite lost its SENPOT device on 2 September 1999. All RPA datasets past this day (including our day of interest) are unreliable during sunlit periods due to the unknown negative charging of the sensor. Due

to the terminator position on our day of interest, this makes measurements from roughly half of F14's track useless. In addition, the F12 satellite's operational lifetime ended in April 1997. While the sensors continued to function until June 2002, reliable data are, at times, sporadic.

The above limitations effectively reduced the utility of many of the F12 datasets during our day of interest, and limited useful data from F14 to the dark part of the satellite's track during the same period, or only the first one-third of the high-latitude dataset. Additionally, there is a 101 minute period between each satellite's topside pass of the north polar regions. Since we are attempting to identify some features which may occur over time scales of only tens of minutes before a change in the convection pattern modifies them, a satellite track over the high-latitude ionosphere must occur very near our time of interest in order to be comparable to our simulation calculations. Indeed, many of our runtimes were chosen because of their valuable IMF traits. In some cases, the closest polar satellite crossing was 30 minutes before or after the model run time. In addition, it takes the satellite roughly 20 minutes to pass from the 50° low latitude boundary of the TDIM on the dusk side to the 50° low latitude boundary of the TDIM on the dawn side. This means that even if we find a satellite pass which moves over the pole at exactly our model run time, the early and late stages of the pass are observed 5-10 minutes before and after the model run time, respectively. This limited our confidence in comparing the short time scale features (like those occurring during fleeting Bz southward periods) with in-situ data. Finally, the satellites provide observations from a one-dimensional line of the topside ionosphere. This line of observations does not necessarily correspond to density features that develop due to certain ionospheric

conditions and due to some convection patterns. We will use an F15 track as an example. This F15 track begins its trek across the northern geographic high latitudes ascending north of magnetic 50° latitude near 2000 MLT. It continues toward morning, passing the noon-midnight meridian at around 70° magnetic latitude. The satellite exits the high latitudes when it moves south of 50° near 1000 MLT. This path is illustrated in Figure 3.10. Because the RPA measures ion density at only single points in space every four seconds along the satellite's path, we end with a one-dimensional line of density data. In order to make reasonable conclusions about the reliability of our simulated density calculations, we must look for easily identifiable plasma density structures along this one-dimensional line. However, the orientation of these structures could be such that they do not cross the track of our observational platform, or they could be aligned with the path so that the density within the structure is measured along the entire path, thus confusing the results. More of this limitation will be discussed in the next subsection when we cover specific, identifiable density structures.

Our review of validation limitations has uncovered a few challenges in using in-situ data from DMSP satellites. These challenges will leave us a restricted set of comparable in-situ datasets. Despite the limitations, the DMSP measurements represent one of our only direct comparison choices for plasma density in the high-latitude ionosphere, and useful comparisons are still possible. We will revisit this issue in our results chapter.

3.4.2. Density Structures Valuable for Comparison Studies.

Having discussed the in-situ data platform, we proceed to a discussion of high latitude top-side ionospheric density structures that lend themselves to comparisons

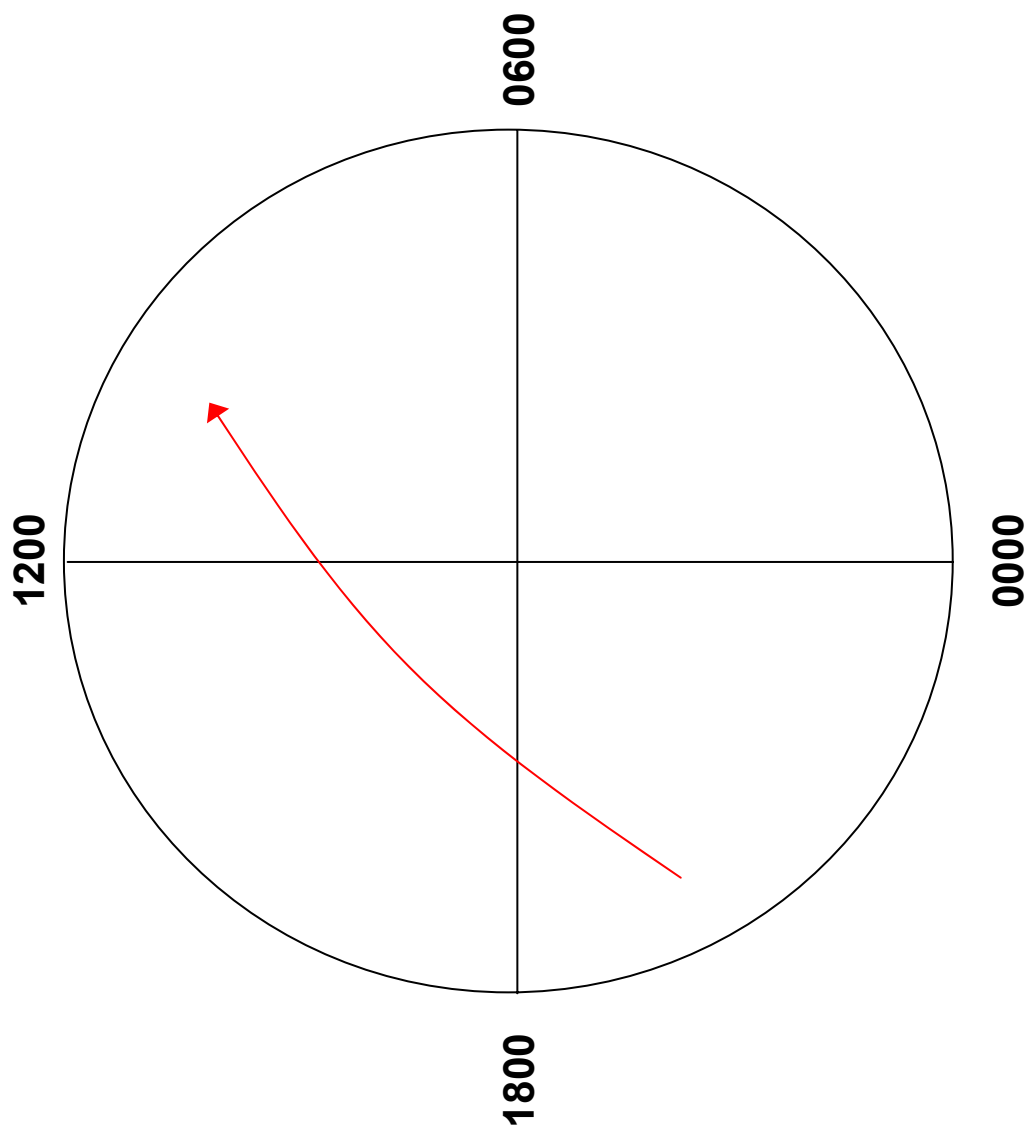


Figure 3.10. An example of an F15 satellite pass over the northern high latitudes. Note that the one-dimensional availability of observations makes generalizations concerning agreement between in-situ densities and simulated densities difficult.

among our three density mappings: simulated density results from statistical convection inputs, simulated density results from SuperDARN convection inputs, and DMSP in-situ satellite observations. Obviously, simulated structures that do not occur across the available DMSP satellite tracks cannot be used for comparison with in-situ data. We will, however, use these when possible for comparison between simulation results using the different convection inputs. In addition, we may not be able to use density structures which occur only during major geomagnetic storms, as our period of interest does not qualify as such.

3.4.2.1. Low-Density Features.

Groves [2002] in his dissertation discusses many features he has found in his parameterization studies: some through a thorough literature review, and some through countless simulation runs. Principal low-density structures which occur during minor events such as ours are polar holes, enhanced ion drift (EID) troughs, and sub-cleft depressions. While polar holes and EID troughs have been discussed in previous studies by Hoegy and Grebowsky [1991] and Schunk and Sojka [1982a] respectively, sub-cleft depressions are introduced by Groves [2002] for the first time. We will touch on all three here. Polar holes are found in the anti-sunward end of the polar cap. While the definitive mechanism behind polar hole formation is still in dispute, Groves [2002] builds a strong case that the very low densities have been caused by downward $\mathbf{E} \times \mathbf{B}$ drift, commonly found in the standard two-cell convection pattern as the anti-sunward moving plasma moves away from the magnetic pole and the earth's magnetic field becomes sufficiently non-vertical. EID troughs, as the name suggests, have been shown to be produced by increased ion temperatures due to high-speed channels of horizontal plasma flow

associated with strong convection electric fields. Schunk and Sojka [1982] focused on the high temperatures produced in these situations, while Groves [2002] adapted this concept to identify density features produced by the elevated temperatures. Sub-cleft density depressions, on the other hand, can only occur under steady, weak plasma drift. Downward neutral wind-induced field-aligned air drag near the noon meridian outside the convection pattern can produce this feature. Even though densities may still be high in these features due to photoionization, the density is still relatively small compared to high-density structures which often occur in the same general area.

3.4.2.2. High-Density Features.

While fewer in number, high-density features are perhaps the best features for use in comparison studies. During storm time, the F-layer ionosphere often has a reduced density profile across much of the high-latitudes. A band of high densities can be easily identified and used for comparison in this case. In the topside, high-density features are often the easiest structures for study, since their presence at these altitudes (near 800 km, for example) is usually due to a transport process that occurred during a dynamic storm-time incident. High-density structures which will be valuable to discuss in this research are tongues of ionization (TOI), both in the dusk convection cell and also in the dawn cell.

TOIs form when plasma from lower latitudes is transported through convection into the higher latitudes, as illustrated by Sojka [1998]. Groves [2002] claims, in its poleward transit, the plasma is lifted significantly through upward vertical $\mathbf{E} \times \mathbf{B}$ drift to much higher altitudes where recombination rates are significantly lower. A continuation of this flow can build up a narrow band of higher equilibrium plasma densities along the

channel of ionospheric convection. Many times, due to the structure of the convection pattern, the width of a TOI can be small as a higher speed channel of poleward convection will produce much more vertical drift than moderate speed poleward convection. Groves [2002] also conclusively demonstrates that there can be a TOI located in the dawn convection cell in addition to the standard TOI often found in the evening cell, and whether this secondary TOI will occur depends entirely upon the geometry of the convection pattern. While the duskside sunward-moving plasma often maintains a slight poleward motion as it travels toward the noon meridian, the dawn plasma many times does not. Our simulation results located in the next chapter will illustrate the relative importance of the two TOIs in our comparison study.

IV. Results and Conclusions

Having discussed how we chose the study day, picked the four simulation run times, and reviewed how we fed our input data into the TDIM, we now display our resulting density maps and develop conclusions from these results. We will begin by highlighting similarities and differences between the results using statistical inputs and the results using SuperDARN inputs. We will also discuss what we should have expected to find in our results using Groves [2002] conceptual density structure parameterization (DSP) technique. We will proceed with a comparison of the simulation top-side ionospheric density results with DMSP in-situ data, keeping in mind a few of the limitations we discussed in the previous chapter. Finally, we will develop conclusions based upon the results achieved here, and possibilities for future work will be provided.

4.1. Results and Analysis

We begin our analysis with simulation results displayed side-by-side using our two input electric field models. Figures 4.1, 4.2, 4.3, and 4.4 show density values calculated by TDIM in the topside ionosphere at 800 kilometers at our four runtimes of 0400 UT, 1240 UT, 1648 UT, and 2030 UT, respectively.

4.1.1. 0400 UT Results.

Figure 4.1 shows 800 km plasma density results for the 0400 UT run time. The left dial shows TDIM-SuperDARN results, while the right dial shows TDIM-statistical results. Each dial has the same DMSP in-situ density values superimposed on the plot. The DMSP values are for the F15 satellite, with the satellite ascending into the evening

DMSP-Model Comparison

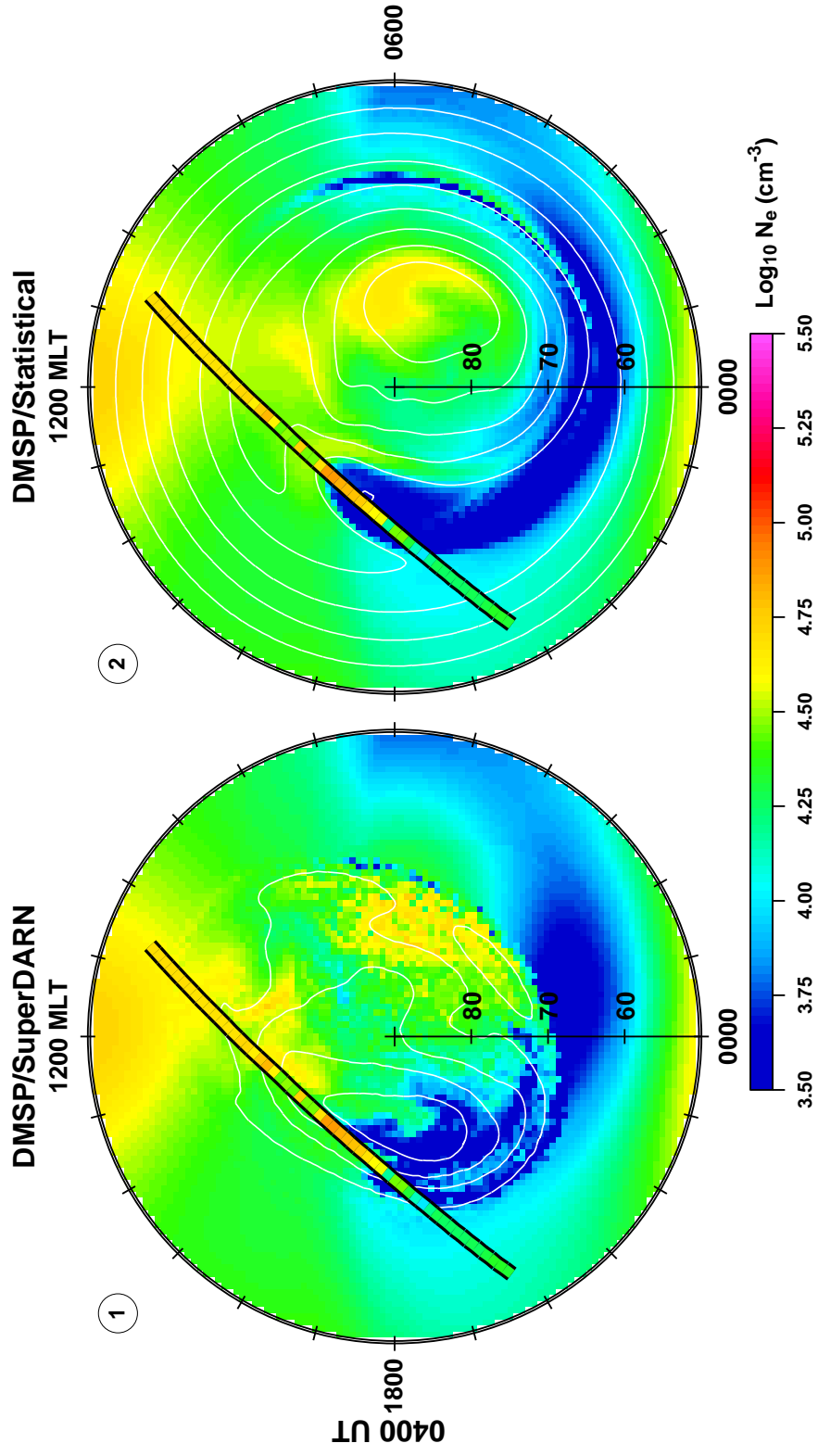


Figure 4.1. 0400 UT TDIM simulation results for an altitude of 800 km using SuperDARN inputs (left) and statistical inputs (right). The input convection pattern is displayed using white contours (5 kV spacing) and the DMSP in-situ measurements are displayed along the satellite's track. The satellite in use here is F15, and the in-situ data has been averaged into 20-second bins.

DMSP-Model Comparison

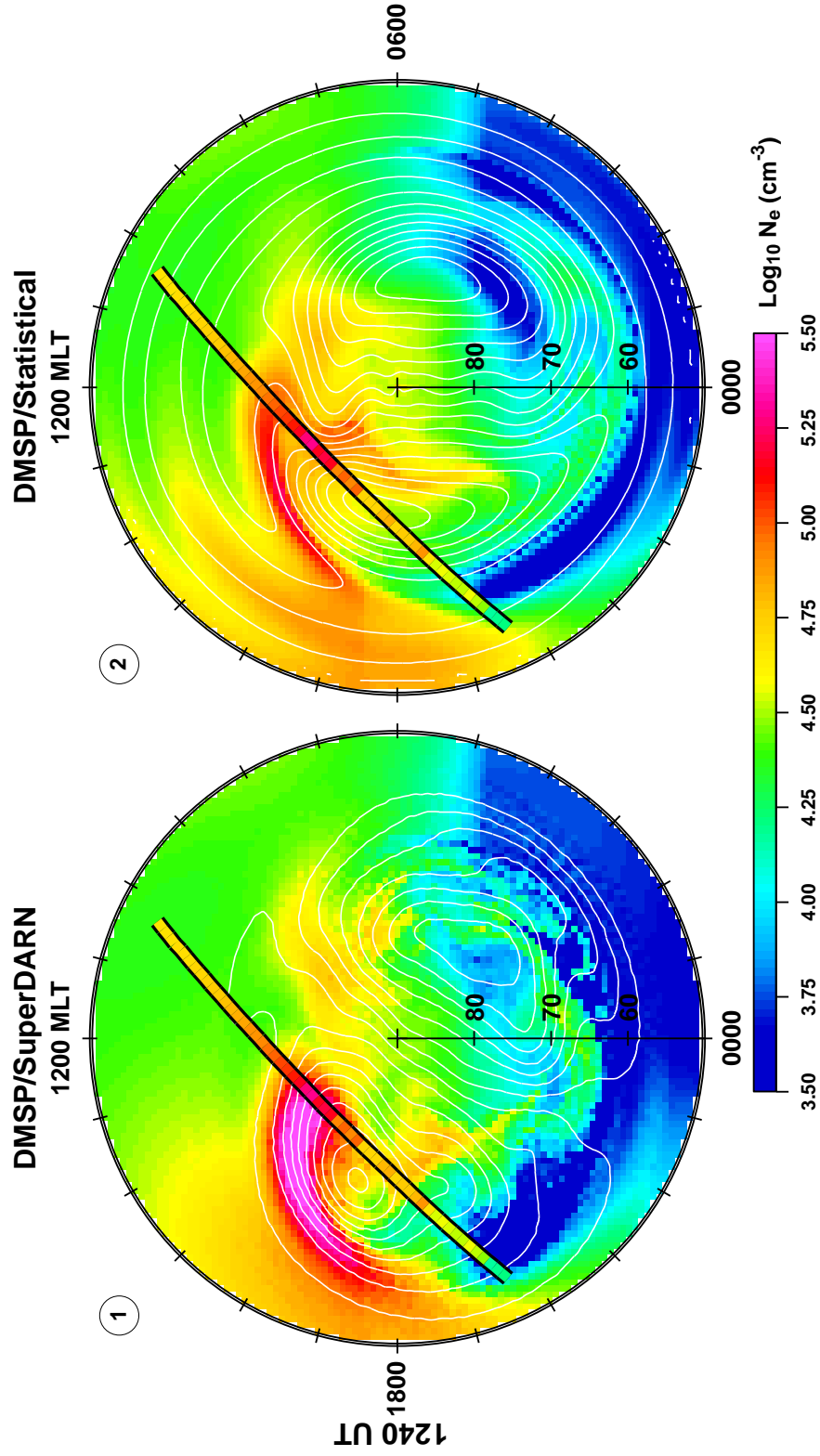


Figure 4.2. 1240 UT TDIM simulation results for an altitude of 800 km using SuperDARN inputs (left) and statistical inputs (right). The input convection pattern is displayed using white contours (5 kV spacing) and the DMSP in-situ measurements are displayed along the satellite's track. The satellite in use here is F15, and the in-situ data has been averaged into 20-second bins.

DMSP-Model Comparison

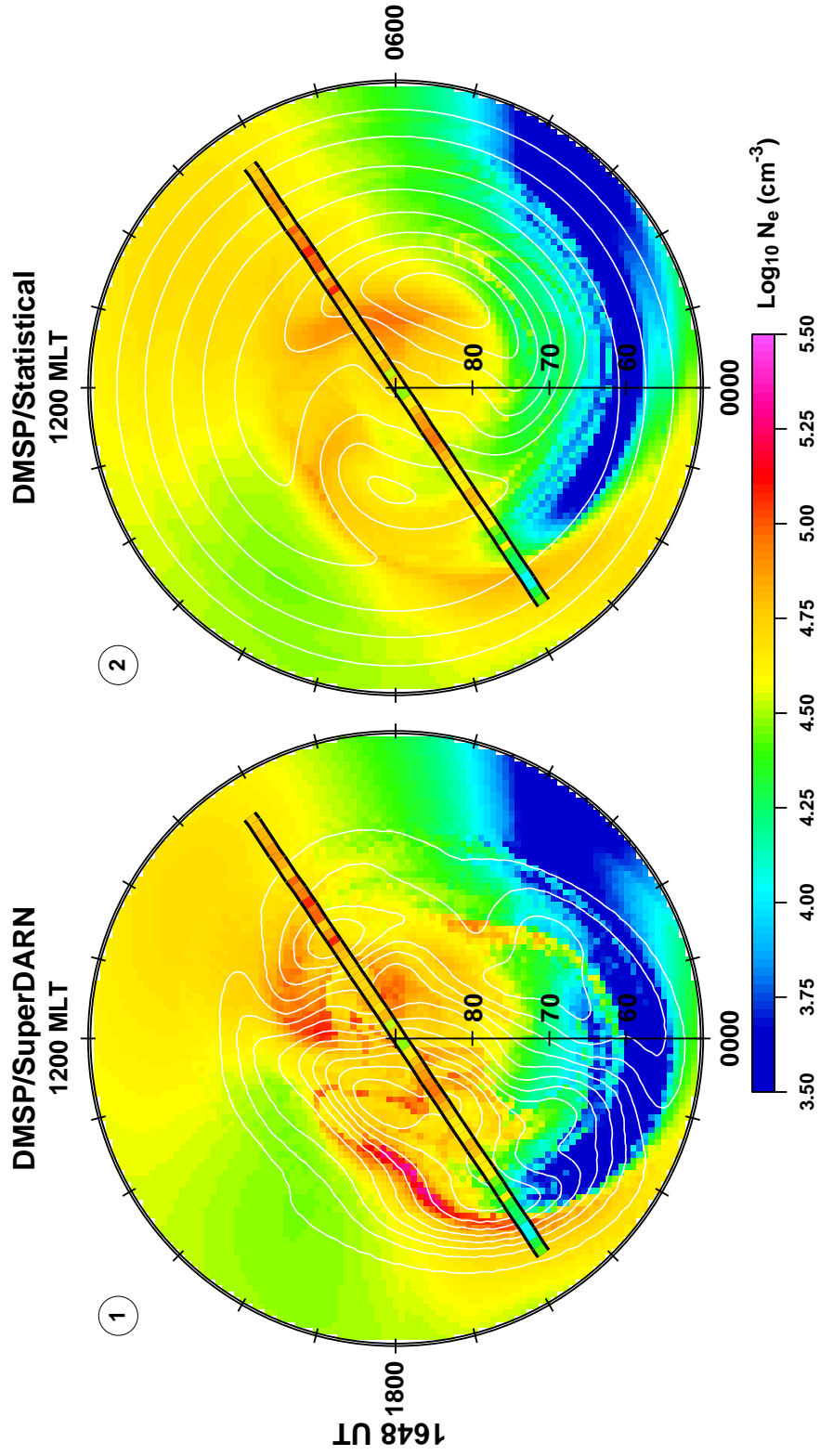


Figure 4.3. 1648 UT TDIM simulation results for an altitude of 800 km using SuperDARN inputs (left) and statistical inputs (right). The input convection pattern is displayed using white contours (5 kV spacing) and the DMSP in-situ measurements are displayed along the satellite's track. The satellite in use here is F12, and the in-situ data has been averaged into 20-second bins.

DMSP-Model Comparison

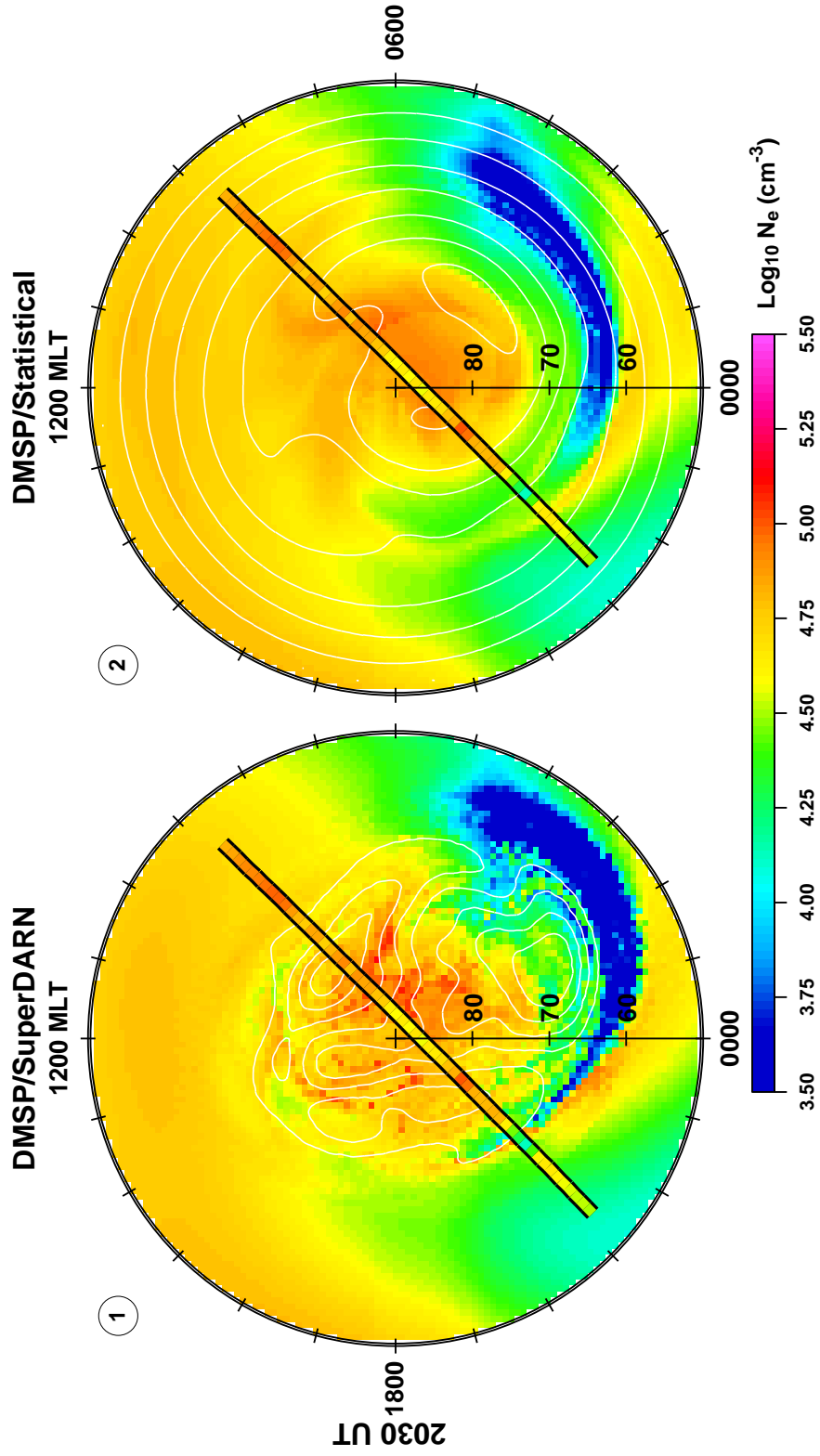


Figure 4.4. 2030 UT TDIM simulation results for an altitude of 800 km using SuperDARN inputs (left) and statistical inputs (right). The input convection pattern is displayed using white contours (5 kV spacing) and the DMSP in-situ measurements are displayed along the satellite's track. The satellite in use here is F15, and the in-situ data has been averaged into 20-second bins.

sector at 0338 UT, crossing the noon-midnight meridian at 0353 UT, and exiting the morning sector at 0400 UT.

The plots in Figure 4.1 show a comparably low density top-side ionosphere as compared with the other run times. This is due to the solar terminator position from approximately 1730 MLT to 0500 MLT. The terminator can be found in this approximate fashion by looking for the change between the green shading and the blue shading. The convection patterns are superimposed in white. The difference between the two patterns is apparent as we discussed in the previous chapter, with the dawn convection cell dominating the statistical pattern (right dial) while the dusk cell dominates the SuperDARN pattern (left dial). We initially see that both density maps contain the same general features. We can attribute this to the fact that with very weak convection patterns across the high latitudes, the dominant parameters in obtaining density equilibrium are photoionization (production) and charge-exchange and recombination (loss). Indeed, high-latitude convection is only producing minor, second-order effects due to weak electric fields. Two features resulting from the convection will be discussed here. The first feature is found on both plots. It is located near the noon-midnight meridian on the sunward side of the pole at approximately 80° and is a minor density enhancement near the convection reversal. The SuperDARN run shows two distinct enhancements, one near the dusk convection reversal and one near the dawn convection reversal. The statistical run did not create the enhancement on the dusk side of the noon-midnight meridian. The second density feature, also present on both dial plots, is located near dawn at roughly $75\text{--}85^\circ$, and is also a density enhancement. In both cases, the placement of the dawn convection cell allows a long, slightly poleward drift of

plasma from night to day. This lifts the plasma and produces the TOI. To some small degree, the speckled nature of the SuperDARN results is likely due to remnant artificial small-scale turbulence in the pattern due to our imperfect two-dimensional interpolation of raw data.

While the DSP conceptual technique developed by Groves [2002] was created for geomagnetic storm-time conditions, his general ideas can still be applied in non-storm circumstances to provide a further basis for model comparisons. In this case, for example, the technique would predict the midnight, 50° density enhancement due to upward drift of plasma from neutral wind-induced field-aligned air drag simultaneous with a sustained period of preceding quiet flow conditions. Such an enhancement is present on both model runs in Figure 4.1.

We can see from the DMSP data shown on Figure 4.1 that both models did reasonably well along the ends of the track. However, both runs contain a major discrepancy near dusk side of the terminator, as a swath of high-density plasma was measured by the F15 satellite. Turning to Groves [2002] conceptual method for help in judging relative model performance, we can suggest several things. Based on the Kp/IMF selection rules, and also the recent non-dynamic conditions in the hours preceding 0400 UT (see Figure 3.1), the statistical electric field has no way of producing this swath, as the enhanced densities are located directly over the center of the weak dawn convection cell where plasma flow is stagnant and not sunlit. However, the SuperDARN result perhaps is not too far from developing the in-situ feature. Relatively moderate plasma flow is found on the equatorward edge of the dusk cell. While SuperDARN has found this flow to be mostly zonal, or non-poleward, a slight

modification of the pattern here could produce a moderate poleward flow component which would lift plasma from the F-layer into the topside at roughly this location. This could lead to a high-density TOI at 800 km in the same approximate location as F15 found it. As further support for this possibility, we note that the raw SuperDARN data on this portion of the equatorward edge of the convection pattern shows no actual returned radar transmissions. This is illustrated in Figure 4.5, taken from the SuperDARN website. The pattern at this data-sparse location was created by forcing a continuous plasma flow between actual measurements. Further possible evidence of the better performance of the SuperDARN pattern is seen by noting that the convection reversal region shows enhanced density due to a poleward-directed dusk cell convection channel only on the SuperDARN model run. This is verified by elevated in-situ measurements near 1300 MLT at roughly 75° latitude in the DMSP data track.

4.1.2. 1240 UT Results.

Figure 4.2 displays 800 km plasma density results for the 1240 UT run time. The left dial again shows TDIM-SuperDARN results, while the right dial shows TDIM-statistical results. The DMSP values are for F15, with the satellite ascending into the evening sector at 1214 UT, crossing the noon-midnight meridian at 1228 UT, and exiting the morning sector at 1235 UT. Note that the general location of the solar terminator has shifted significantly from the 0400 UT run, lying approximately along a line from 1900 MLT on the left side of the dials to 0500 MLT on the right side of the dials. Thus, a much larger fraction of the high-latitude ionosphere is sunlit at this 1240 UT runtime.

Figure 4.2 shows a fairly strong global convection pattern has resulted from a lengthy (2-3 hour) period of Bz southward IMF conditions preceding the 1240 run time.

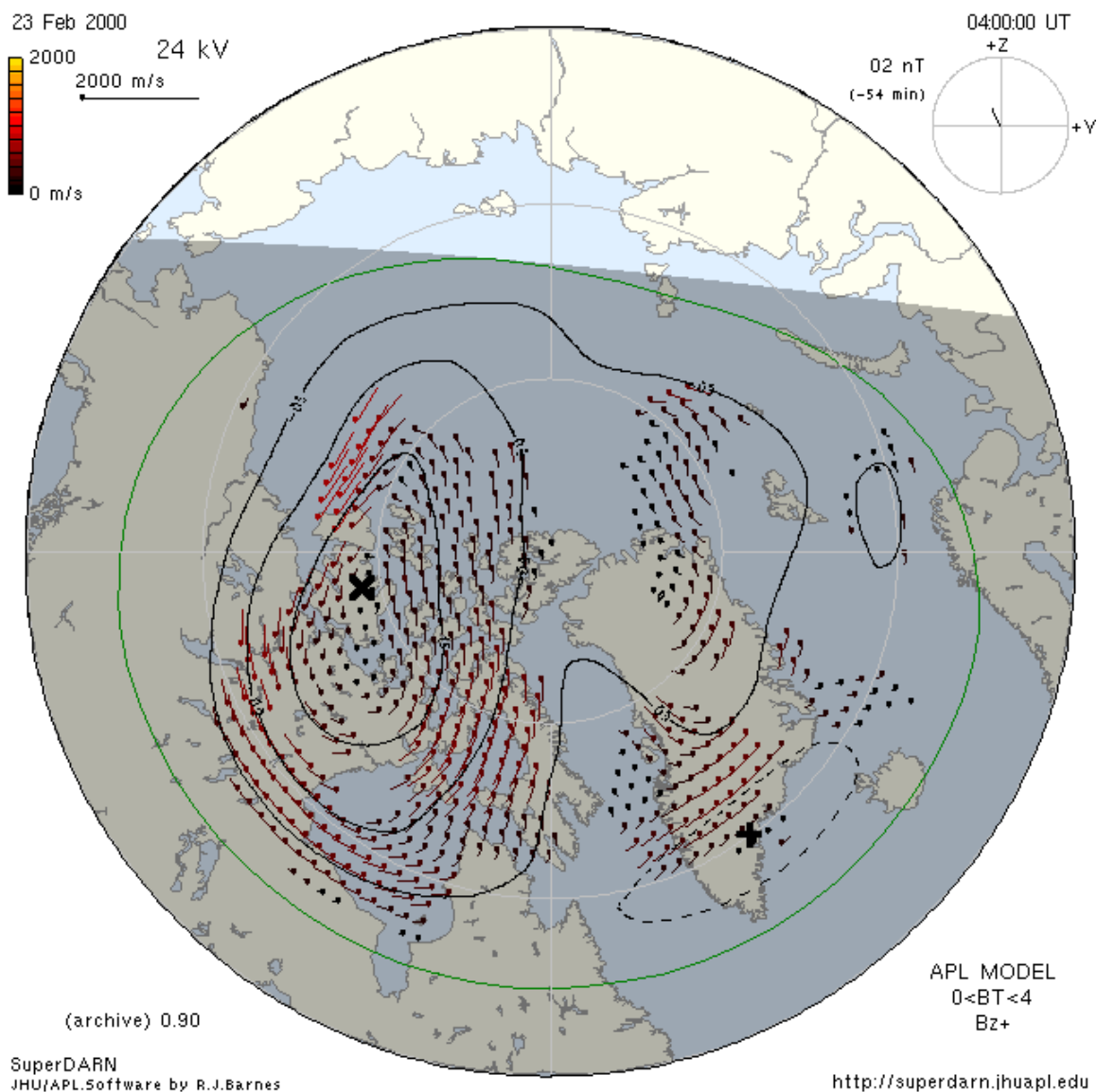


Figure 4.5. Averaged raw velocity data returned to SuperDARN in the 2 minutes preceding 0400 UT. Lines of latitude are provided in 10° increments in faint white. The lowest latitude shown is 60° . The direction of plasma flow at each location is away from the point along the flag, while speed is illustrated by the relative flag length. Regions with no points do not have sufficient returns to resolve the velocity [superdarn.jhuapl.edu].

We see that a dusk TOI feature is represented on both model runs. However, each displays this feature differently. The location and late-evening-to-late-morning tilt of the SuperDARN convection pattern has produced a strong poleward component of the flow across a large portion of the dusk latitudes. The highest density regions in the plots, along the outer shoulder of the dusk cell, seem to be sourced in a lower-latitude region near dusk. Foster [1993] referred to this as Storm-Enhanced Density (SED). It is thought that this feature is produced during active conditions where sunward convection in the expanded afternoon convection cell “scoops up” mid-latitude co-rotating plasma and carries it poleward, producing a TOI (in fact, Foster [1993] calls this the “snowplow” effect). The exact location and orientation of the resulting TOI is slightly different in each plot. In Figure 4.2, the SuperDARN run seems to better grasp the width and location of the TOI (compared to the DMSP observations) than did the statistical run. We must note here, however, that the DMSP data are only a one-dimension set of observations. For this reason, we provide Figure 4.6, which overlays a second DMSP satellite track, the track of F13. F13 on this pass ascends into the dusk sector at 1223 UT, crosses the noon-midnight meridian at 1233 UT, and exits the dawn sector at 1244 UT. We see a slightly different story from this pass. The statistical model run here seems to have an outstanding result for the dusk cell TOI, matching nearly perfectly with the in-situ data. This is an excellent example of the limitations of in-situ data comparison.

We now pursue a conceptual discussion to gain further insight into our results. Using the Groves [2002] DSP technique, both model runs do an admirable job of creating expected first-order density effects relating to the dusk cell TOI. However, precise differences in orientation of the central flow channels between the statistical and

DMSP-Model Comparison

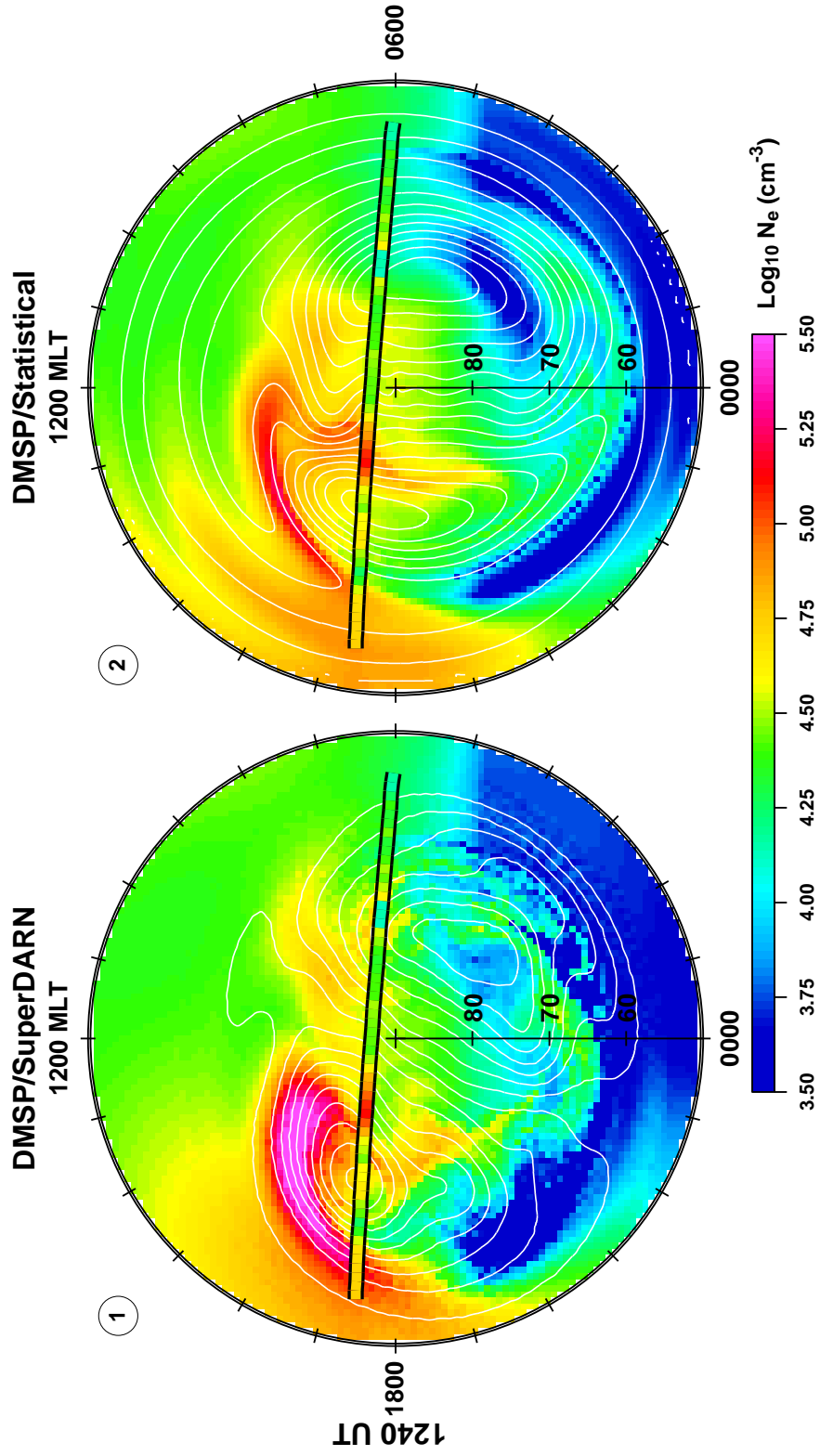


Figure 4.6. 1240 UT TDIM simulation results for an altitude of 800 km using SuperDARN inputs (left) and statistical inputs (right). The input convection pattern is displayed using white contours (5 kV spacing) and the DMSP in-situ measurements are displayed along the satellite's track. The satellite in use here is F13, and the in-situ data has been averaged into 20-second bins.

SuperDARN patterns result in different density structures. For the SuperDARN result, because the central flow channel between the two cells immediately tilts from late morning to late evening following the convection reversal, it loses its poleward component and takes on an anti-poleward component at 1500-1700 MLT near 80° latitude. This causes the high density plasma experiencing vertical lift coming out of the SED to suddenly be forced downward again. Thus, in the SuperDARN run, the TOI dissipates near the convection reversal. Thus, though the SuperDARN run matches well with the F15 DMSP track in Figure 4.2, it does not match well with the F13 track on Figure 4.6. For the statistical pattern, an interesting morphological detail is present. The convection pattern in the central channel near 80° latitude between 1500 and 1600 MLT switches from a morning-to-premidnight sector orientation to an afternoon-to-predawn sector orientation. This causes the SED density enhancements coming into the polar cap to maintain a poleward orientation, thereby maintaining the $\mathbf{E} \times \mathbf{B}$ vertical lift necessary to sustain the TOI. Thus, the statistical pattern actually produces the more accurate result displayed in Figure 4.6 when compared to F13 DMSP data. A final note reveals that a moderate density enhancement, a dawn TOI, has developed in both model runs during the plasma's poleward journey on the dawn side, then quickly deteriorated as it moved anti-poleward across a dusk-dawn line.

4.1.3. 1648 UT Results.

While the possibility of the development of well-defined density features is relatively strong during long-duration Bz-southward IMF conditions, quickly changing conditions bring us doubt. Figure 4.3 shows 800 km plasma density results for the 1648 UT run time. As on the previous plots, the left dial shows TDIM-SuperDARN results,

while the right dial shows TDIM-statistical results. The DMSP values are for the F12 satellite, with the satellite ascending into the evening sector at 1627 UT, crossing the noon-midnight meridian at 1638 UT, and exiting the morning sector at 1650 UT. A strong Bz-south component of near 15 nT has developed rapidly and only occurs in the 20-minutes prior to our run time. We note here that with the two-minute cadence of the SuperDARN patterns into TDIM, 10 SuperDARN convection patterns representing the strong Bz-south component have been utilized by the model. Thus, the SuperDARN data's resolution has enabled the TDIM to properly reflect the short period of southward IMF. Figure 4.3 illustrates this. On both plots, our SED feature, which developed near the 1240 UT run time, has co-rotated to the late evening hours: well past sunset and into the nightside ionosphere. This remarkably persistent feature has been maintained due to the low recombination rates in the topside and also the very quiet geomagnetic conditions between the 1240 UT run and the start of the southward IMF conditions preceding the 1648 UT run. Our SuperDARN-measured convection pattern has quickly expanded due to the relatively strong southward IMF conditions and has dipped into the remnant SED feature once again. This process on the SuperDARN run is very efficient, since the dusk convection cell is centered on the nightside of the dusk-to-dawn line. This has produced a long TOI structure as the plasma flows slightly poleward during its journey sunward. The statistical convection pattern, much-weaker due to the small Kp scaling we discussed in the previous chapter, does not efficiently reach into the co-rotated SED and therefore has not produced such a pronounced dusk TOI. Both models, through moderate poleward convection near the dawn reversal, have produced dawn TOIs. The TDIM-SuperDARN density result, however, contains a pocket of reduced density just sunward

of the pole near 0900 MLT. The Groves [2002] DSP technique does not provide an explanation for such second-order features, so we must conclude the result is developed morphologically from a prior time period. While the true cause of feature is unknown, its presence does illustrate how the use of high resolution SuperDARN convection patterns can result in modeling significant smaller scale features that are not developed during the model run driven by the statistical convection patterns.

We proceed with a conceptual discussion of the first-order features found in this simulation density result. Groves' [2002] DSP technique does produce both TOIs correctly. However, again due to unknown previous conditions, there is a feature which cannot be ascertained. On the SuperDARN map, the dusk TOI extends back toward the dusk-dawn line at around 80° . Since this extends the high-density plasma directly through the center of the dusk convection cell, we must assume that it is present from prior, different electric field patterns. This is understandable, as our pattern here has developed from a less active pattern in just a 20-minute period. The DMSP F12 data plotted here suggests some agreement between the SuperDARN run and in-situ data. The extension of the dusk TOI through the center of the dusk convection cell seems to be justified, according to the DMSP data. The statistical run, however, displays lower plasma densities in this region and thus does not match with the in-situ measurements. Thus, while the SuperDARN run's dusk TOI seems to be verified, the dawn TOI does not match with in-situ data.

It is also interesting to note that in a separate region of the DMSP track, comparison of model runs with in-situ data produces definitely mixed results. If we examine the DMSP track as it passes near the outer, 70° edge of the dawn convection cell

near 0800 MLT, the satellite encounters a highly structured high-density environment. While neither model run reproduced this feature, it appears the TDIM-statistical run fared worse, as the spatially contracted convection pattern cannot develop any features at colatitudes greater than 15° , as only co-rotation occurs in this region. From Figure 3.1 we note that K_p and the IMF B_y component did not vary dynamically during this short duration event. Therefore, selection rules for Heppner-Maynard patterns would not have introduced any convection dynamics capable of producing such a highly structured region displayed in the model result. Again, though not precisely placed at this time, the SuperDARN result for 1648 UT does at least reproduce smaller-scale density enhancements throughout the polar cap, rather than simply smooth, large-scale features as in the statistical run.

Though first-order features such as the dusk TOI seem to be verified adequately in the SuperDARN run when compared to DMSP data using the Groves [2002] DSP technique, one specific part of the polar cap density structure does not seem to match with conceptual arguments. Using Groves' technique, the dusk TOI should penetrate through the poleward central flow channel near noon all the way into the sunlit polar cap. However, this region near the pole on the DMSP data contains a small-scale patch of relatively lower plasma density. It is impossible to theorize exactly how such a feature would develop. Additionally, it is likely that the abrupt nature of the convection pattern's development just before the run time at 1648 UT results in dynamics which TDIM cannot adequately model.

4.1.4. 2030 UT Results.

Finally, we conclude our results analysis with the 2030 UT runtime results found in Figure 4.4. As previously, the left dial shows 800 km plasma density results for the TDIM-SuperDARN run, while the right dial shows TDIM-statistical results. The DMSP values on Figure 4.4 are for the F15 satellite, with the satellite ascending into the late evening sector at 2039 UT, crossing the noon-midnight meridian at 2049 UT, and exiting the morning sector at 2101 UT. While the satellite passes the high latitudes nearly 20 minutes after our 2030 runtime, we note from Figure 3.1 that the IMF Bz component is strongly positive and fairly steady for the 3-4 hours preceding the runtime, and the IMF By component has had only minor variations. Thus we would expect few morphological differences to develop during this time.

At first glance, we note that dayside ambient plasma density after this period of sustained, strong Bz northward conditions is nearly two times higher than the ambient dayside plasma at 1240 UT, our runtime which followed a period of sustained Bz southward conditions. Since the IMF has a northward orientation, the convection pattern on both the SuperDARN and the statistical run is contracted mostly poleward of 70° . Since the terminator is located at approximately 80° on the nightside of the pole, a majority of the polar cap is sunlit and contains plasma densities ranging from 6×10^4 to 10^5 cm^{-3} . The combination of strong photoionization and generally weak convection limits our ability to locate distinct plasma features on our simulation density results. We can locate, however, the continued co-rotation of the SED feature developed at approximately 1240 UT. Indeed, the feature has moved roughly eight hours of magnetic local time to near 0000 MLT. This co-rotation has produced a startling density gradient

near the location of the mid-latitude density trough in the midnight sector near 60° latitude on both simulation plots. Conceptually, this feature should indeed be present if the convection pattern for the previous eight hours does not dissipate the SED. In the absence of previous convection effects for the entire day, topside plasma density in the midnight sector would be expected to be fairly symmetric and low density on either side of midnight MLT.

We note a slight representation of a small-scale dawn TOI on the SuperDARN result near 0600 MLT due to moderate poleward flow around the anti-sunward boundary of the reversed convection cell centered at 0900 MLT near 80° . We also note a narrow high-density dusk tongue in the afternoon near 85° . This seems to have resulted again from vertical $\mathbf{E} \times \mathbf{B}$ drift, this time around the dusk side of the reverse convection cell centered just duskward and sunward of the magnetic pole. Neither of these features can be found in the statistical result, as the statistical convection pattern input into TDIM was weak and smoothed due to the averaged nature of the pattern.

While the DMSP in-situ information is generally smooth, we do see a suggestion of fine-scale detail during this run. We also note evidence of our co-rotating SED feature. This is found near the beginning of the satellite's ascent in late evening. While the placement is slightly different, it is encouraging to find a feature that conceptually verifies over several previous simulation runs.

4.2. Conclusions and Possibilities for Future Work

We began this research with the hope of expanding upon the relatively small collection of studies using various electric field inputs to run large ionospheric

simulations and comparing results with conceptual expectations and in-situ measurements. Both statistical electric fields and SuperDARN-derived electric fields were used as inputs to the TDIM. Generally, we conclude that the TDIM-SuperDARN runs produced more accurate density results than the TDIM-statistical runs. The increased accuracy resulted using both the comparisons with conceptual model results and from the comparisons with in-situ measurements.

A number of findings in our simulations were especially encouraging. A newly-defined dawn tongue of ionization, simulated and discussed by Groves [2002], was again simulated in this research. Many morphological features were simulated to include SED, dusk-cell TOI, and also the persistent co-rotation of these features in quiet geomagnetic conditions. In our SuperDARN simulations, small-scale patches were simulated during rapidly changing IMF conditions, although in-situ verification of these features was indeed difficult. During the 1648 UT run (Figure 4.3), a very narrow TOI was developed in the TDIM-SuperDARN run that could not be developed by TDIM-statistical run due to the lack of fine resolution. In fact, many of the concepts discussed by Groves [2002] within the construct of the DSP technique have been found in this study. One such concept was the importance of poleward or anti-poleward motion in developing vertical $\mathbf{E} \times \mathbf{B}$ drift in the mid- to high-latitude ionosphere. This concept was ironically illustrated with our artificially turbulent SuperDARN convection patterns before the smart-interp method was applied. Rapid upward and downward drift developed in the wavy convection pattern, which resulted in high- and low-density patches in the early simulation density results. Another such concept was the importance of neutral wind-induced field-aligned air drag under long periods of quiet geomagnetic conditions. These

conditions occurred often during our study day, and the relevance of air drag was discovered before our elimination of auroral precipitation from the model runs. To prove the relevance of this parameter, the artificial density enhancement in the topside auroral zone was eliminated by the temporary removal of neutral winds from the simulation run. This was displayed in Figure 3.9 and proved that neutral winds are indeed a first-order parameter during quiet geomagnetic conditions, as claimed by Groves [2002].

Many of the conclusions developed during this research were cultivated before the final TDIM runs were completed. We covered early in the previous chapter the difficulty we faced in building a proper interface between the SuperDARN raw data and the TDIM. While our smart-interp method was generally successful, there are more rigorous mathematical methods to develop this interface. We reviewed in the background chapter the major work accomplished in recent years using the MHD model's self-consistent convection and auroral inputs and statistical patterns [Sojka et al., 1998] and the simulation work using AMIE, MHD, and statistical patterns [Groves, 2002]. While we used a very different case study due to the relative youth of the SuperDARN radar network, we believe our results are, in a limited sense, consistent with the findings of the earlier studies. The SED and the TOIs developed under similar circumstances. However, many of our results are unique due to the relatively quiet geomagnetic nature of 23 February 2000, as compared to the storming during the former case studies. One such unique result was the long-duration of the co-rotating SED feature. The earlier studies could not have produced such results, as the strength of the convection pattern during these studies eliminated co-rotation as a first-order parameter.

We also faced several challenges during this research effort. One such challenge we faced was the uncoupled nature of our input datasets. We discussed in the methodology chapter the limitations of using independent auroral precipitation and convection patterns. This required us to remove auroral precipitation completely from our simulation. This was possible since we were only analyzing results in the topside ionosphere, at altitudes (near 800 km) where precipitating electrons should have negligible effects. Another challenge was found with changing convection patterns over small areas and during short time scales, as many researchers would expect. In this study, the convection patterns input into the TDIM were of a finer resolution than the inputs used in earlier studies, both temporally and spatially. While the fine resolution of the data introduced a few challenges, such as attempting to verify density results with in-situ measurements, first-order plasma features were still produced by the simulations and indeed could be verified by the satellite data and by comparison with conceptual models.

Finer resolution electric fields provide many advantages to possible future work with small-scale density patches and scintillation effects. Future expansion in the number of radars in the SuperDARN network should improve the reliability of their data further, and produce better results during large geomagnetic storms when the equatorward boundary of the convection pattern and of the aurora extends beyond the minimum latitude of the currently existing network. However, continued studies using less geomagnetically active study days is still valuable, as conclusions made from these studies can be applied in an appropriately scaled manner to more active conditions. A study using many more model runtimes, while currently time consuming and computationally taxing, would improve our knowledge of the time development and

spatial transport of density features. Combining the high-resolution capability of the SuperDARN radar network with observations of actual auroral strength and coverage would solve the significant issue of inconsistent auroral precipitation and E-field convection patterns. Current work to combine many sets of thermospheric, ionospheric, and magnetospheric measurements would immensely improve our ability to create a self-consistent picture and even increase the spatial coverage of “global” measurements to all locations around Earth.

Bibliography

- Baker, K. B., and S. Wing, A new magnetic coordinate system for conjugate studies of high latitudes, *J. Geophys. Res.*, *94*, 9139-9143, 1989.
- Bristow, W. A., J. M. Ruohoniemi, and R. A. Greenwald, Super Dual Auroral Radar Network observations of convection during a period of small-magnitude northward IMF, *J. Geophys. Res.*, *103*, 4051-4061, 1998.
- Emery, B. A., G. Lu, E. P. Szuszczewicz, A. D. Richmond, R. G. Roble, P. G. Richards, K. L. Miller, R. Niciejewski, D. S. Evans, F. J. Rich, W. F. Denig, D. L. Chenette, P. Wilkinson, S. Pulnits, K. F. O'Loughlin, R. Hanbaba, M. Abdu, P. Jiao, K. Igarashi, B. M. Reddy, Assimilative mapping of ionospheric electrodynamics in the thermosphere-ionosphere general circulation model comparisons with global ionospheric and thermospheric observations during the GEM/SUNDIAL period of March 28–29, 1992, *J. Geophys. Res.*, *101*, 26,681–26,696, 1996.
- Fedder, J. A., and J. G. Lyon, The solar-wind-magnetosphere-ionosphere current-voltage relationship, *Geophys. Res. Lett.*, *14*, 880-883, 1987.
- Fedder, J. A., and J. G. Lyon, The Earth's magnetosphere is 165 R_E long: Self-consistent currents, convection, magnetospheric structure, and processes for northward interplanetary magnetic field, *J. Geophys. Res.*, *100*, 2623-3635, 1995.
- Fedder, J. A., J. G. Lyon, S. P. Slinker, and C. M. Mobarry, Topological structure of the magnetotail as a function of interplanetary magnetic field direction, *J. Geophys. Res.*, *100*, 3613-3621, 1995a.
- Fedder, J. A., S. P. Slinker, J. G. Lyon, R. D. Elphinstone, Global numerical simulation of the growth phase and the expansion onset for a substorm observed by Viking, *J. Geophys. Res.*, *100*, 19,083–19,094, 1995b.
- Foster, J. C., Storm time plasma transport at middle and high latitudes, *J. Geophys. Res.*, *98*, 1675-1689, 1993.
- Freeman, M. P., C. J. Farrugia, L. F. Burlaga, M. R. Hairston, M. E. Greenspan, J. M. Ruohoniemi, R. P. Lepping, The interaction of a magnetic cloud with the Earth: Ionospheric convection in the northern and southern hemispheres for a wide range of quasi-steady interplanetary magnetic field conditions, *J. Geophys. Res.*, *98*, 7633–7656, 1993.
- Greenwald, R. A., K. B. Baker, R. A. Hutchins, and C. Hanuise, An HF phased-array radar for studying small-scale structure in the high-latitude ionosphere, *Radio Science*, *20*, 63-79, 1985.

Greenwald, R., W. Bristow, G. Sofko, C. Senior, J. Cerisier, and A. Szabo, Super dual auroral radar network radar imaging of dayside high-latitude convection under northward interplanetary magnetic field: Toward resolving the distorted two-cell versus multicell controversy, *J. Geophys. Res.*, *100*, 19,661–19,674, 1995.

Groves, C. M., Density structure parameterization of the mid- to high-latitude ionosphere, Dissertation, Utah State University, 2002.

Hardy, D. A., M. S. Gussenhoven, R. Raistrick, and W. J. McNeil, Statistical and functional representations of the pattern of auroral energy flux, number flux, and conductivity, *J. Geophys. Res.*, *92*, 12275–12294, 1987.

Hedin, A. E., MSIS-86 thermospheric model, *J. Geophys. Res.*, *92*, 4649–4662, 1987.

Hedin, A. E., N. W. Spencer, M. A. Biondi, R. G. Burnside, G. Harnandez, and R. M. Johnson, Revised global model of thermospheric winds using satellite and ground-based observations, *J. Geophys. Res.*, *96*, 7657–7688, 1991.

Heppner, J. P., and N. C. Maynard, Empirical high-latitude electric field models, *J. Geophys. Res.*, *92*, 4467–4489, 1987.

Hoegy, W., and J. Grebowsky, Dependence of polar hole density on magnetic and solar conditions, *J. Geophys. Res.*, *96*, 5737–5755, 1991.

Knipp, D. J., B. A. Emery, A. D. Richmond, N. U. Crooker, M. R. Hairston, J. A. Cumnock, W. F. Denig, F. J. Rich, O. de la Beaujardiere, J. M. Ruohoniemi, A. S. Rodger, G. Crowley, B. H. Ahn, D. S. Evans, T. J. Fuller-Rowell, E. Friis-Christensen, M. Lockwood, H. W. Kroehl, C. G. MacLennan, A. McEwin, R. J. Pellinen, R. J. Morris, G. B. Burns, V. Papitashvili, A. Zaitzev, O. Troshichev, N. Sato, P. Sutcliffe, and L. Tomlinson, Ionospheric convection response to slow, strong variations in a northward interplanetary magnetic field: A case study for January 14, 1988, *J. Geophys. Res.*, *98*, 19273–19292, 1993.

Rich, F., and M. Hairston, Large-scale convection patterns observed by DMSP, *J. Geophys. Res.*, *99*, 3827–3844, 1994.

Rich, F., and N. Maynard, Consequences of using simple analytical functions for the high-latitude convection electric field, *J. Geophys. Res.*, *94*, 3687–3701, 1989.

Richmond, A. D., Assimilative mapping of ionospheric electrodynamics, *Adv. Space Res.*, *12*(6), 59–68, 1992.

Richmond, A. D., and Y. Kamide, Mapping electrodynamic features of the high-latitude ionosphere from localized observations: Technique, *J. Geophys. Res.*, *93*, 5741–5759, 1988.

- Ruohoniemi, J., and K. Baker, Large-scale imaging of high-latitude convection with Super Dual Auroral Radar Network HF radar observations, *J. Geophys. Res.*, *103*, 20,797–20,811, 1998.
- Ruohoniemi, J., and R. Greenwald, Statistical patterns of high-latitude convection obtained from Goose Bay HF radar observations, *J. Geophys. Res.*, *101*, 21,743–21,764, 1996.
- Ruohoniemi, J., R. Greenwald, K. Baker, J. Villain, C. Hanuise, and J. Kelly, Mapping high-latitude plasma convection with coherent HF radars, *J. Geophys. Res.*, *94*, 13,463–13,477, 1989.
- Ruohoniemi, J., R. Barnes, R. Greenwald, and S. Shepherd, The response of the high-latitude ionosphere to the coronal mass ejection event of April 6, 2000: A practical demonstration of space weather nowcasting with the Super Dual Auroral Radar Network HF radars, *J. Geophys. Res.*, *106*, 30,085–30,098, 2001.
- Schunk, R. W., and W. J. Raitt, Atomic nitrogen and oxygen ions in the daytime high-latitude F region, *J. Geophys. Res.*, *85*, 1255–1272, 1980.
- Schunk, R. W., and J. J. Sojka, Ion temperature variations in the daytime high-latitude F region, *J. Geophys. Res.*, *87*, 5169–5183, 1982a.
- Schunk, R. W., and J. C. G. Walker, Theoretical ion densities in the lower ionosphere, *Planet. Space Sci.*, *21*, 1875–1896, 1973.
- Schunk, R. W., W. J. Raitt, and P. M. Banks, Effect of electric fields on the daytime high-latitude E and F regions, *J. Geophys. Res.*, *80*, 3121–3130, 1975.
- Schunk, R. W., P. M. Banks, and W. J. Raitt, Effects of electric fields and other processes upon the nighttime high-latitude F layer, *J. Geophys. Res.*, *81*, 3271–3282, 1976.
- Schunk, R. W., J. J. Sojka, and M. D. Bowline, Theoretical study of the electron temperature in the high-latitude ionosphere for solar maximum and winter conditions, *J. Geophys. Res.*, *91*, 12,041–12,054, 1986.
- Schunk, R. W., and A. F. Nagy, *Ionospheres: Physics, Plasma Physics, and Chemistry*, Cambridge University Press, New York, 2000.
- Shepherd, S., and J. Ruohoniemi, Electrostatic potential patterns in the high-latitude ionosphere constrained by SuperDARN measurements, *J. Geophys. Res.*, *105*, 23,005–23,014, 2000.

Slinker, S.P., J.A. Fedder, J. Chen, J.G. Lyon, Deducing global magnetosphere indices and ionospheric energy input for the storm of January 14, 1988 from an MHD simulation (abstract), EoS Transactions, Fall Meeting Supplement 76, F499, 1995.

Sojka, J., Global scale, physical models of the F-region ionosphere, *Rev. Geophys.*, 27(3), 371–403, 1989.

Sojka, J., R. Schunk, M. Bowline, J. Chen, S. Slinker, and J. Fedder, Driving a physical ionospheric model with a magnetospheric MHD model, *J. Geophys. Res.*, 102, 22,209–22,220, 1997.

Sojka, J. J., R. W. Schunk, M. D. Bowline, J. Chen, S. Slinker, J. Fedder, and P. J. Sultan, Ionospheric storm simulations driven by magnetospheric MHD and by empirical models with data comparisons, *J. Geophys. Res.*, 103, 20669-20684, 1998.

Weimer, D. R., A flexible, IMF dependent model of high-latitude electric potentials having “space weather” applications, *Geophys. Res. Lett.*, 23, 2549-2552, 1996.

Vita

Capt Christopher M. Hogue graduated from Warren Central High School in Indiana. He entered undergraduate studies at Purdue University where he graduated with a Bachelor of Science degree in Atmospheric Science. He was commissioned through the Detachment 220, AFROTC.

After initial air force weather training, Capt Hogue's first assignment was to Little Rock AFB as an instructor meteorologist. While stationed at Little Rock, he deployed to Prince Sultan AB, Saudi Arabia for four months in support of Operations Southern Watch and Desert Fox. Upon his return from Saudi Arabia, he was reassigned to Detachment 10, 7th Weather Squadron, Giebelstadt Army Airfield, Germany where he served as the assistant Staff Weather Officer for the 1st Infantry Division. While stationed at Giebelstadt, he deployed to Eagle Base, Tuzla, Bosnia-Herzegovina for three months in support of Operation Joint Forge. Upon his return from Eagle Base, Capt Hogue was reassigned to Detachment 1, 7th Weather Squadron at Leighton Barracks, Wuerzburg, Germany to initiate and develop the newly created unit there while continuing to support the 1st Infantry Division. While stationed at Wuerzburg, he was deployed to Camp Bondsteel, Kosovo in support of Operation Joint Guardian.

Upon completion of his overseas tour, he entered the Graduate School of Engineering and Management, Air Force Institute of Technology (AFIT). He is currently pursuing a Master of Science degree in Physics at AFIT. Upon graduation, he will be assigned to Peterson AFB to serve as flight commander of the weather flight within the 21st Operations Support Squadron.

REPORT DOCUMENTATION PAGE				Form Approved OMB No. 074-0188	
<p>The public reporting burden for this collection of information is estimated to average 1 hour per response, including the time for reviewing instructions, searching existing data sources, gathering and maintaining the data needed, and completing and reviewing the collection of information. Send comments regarding this burden estimate or any other aspect of the collection of information, including suggestions for reducing this burden to Department of Defense, Washington Headquarters Services, Directorate for Information Operations and Reports (0704-0188), 1215 Jefferson Davis Highway, Suite 1204, Arlington, VA 22202-4302. Respondents should be aware that notwithstanding any other provision of law, no person shall be subject to a penalty for failing to comply with a collection of information if it does not display a currently valid OMB control number.</p> <p>PLEASE DO NOT RETURN YOUR FORM TO THE ABOVE ADDRESS.</p>					
1. REPORT DATE (DD-MM-YYYY) June 2004		2. REPORT TYPE Master's Thesis		3. DATES COVERED (From – To) Jun 2003 – May 2004	
4. TITLE AND SUBTITLE COMPARATIVE STUDY ON THE USE OF COHERENT RADAR-DERIVED ELECTRIC FIELDS VS. STATISTICAL ELECTRIC FIELDS FOR THE INITIALIZATION OF A HIGH-LATITUDE IONOSPHERIC MODEL				5a. CONTRACT NUMBER	
				5b. GRANT NUMBER	
				5c. PROGRAM ELEMENT NUMBER	
6. AUTHOR(S) Hogue, Christopher, M., Captain, USAF				5d. PROJECT NUMBER	
				5e. TASK NUMBER	
				5f. WORK UNIT NUMBER	
7. PERFORMING ORGANIZATION NAMES(S) AND ADDRESS(S) Air Force Institute of Technology Graduate School of Engineering and Management (AFIT/EN) 2950 P Street, Building 640 WPAFB OH 45433-7765				8. PERFORMING ORGANIZATION REPORT NUMBER AFIT/GAP/ENP/04-03	
9. SPONSORING/MONITORING AGENCY NAME(S) AND ADDRESS(ES) Det. 11, SMC (CISF) Attn: Dr. Franklin E. Miller 1050 E. Stewart Ave. Peterson AFB, CO 80914				10. SPONSOR/MONITOR'S ACRONYM(S)	
				11. SPONSOR/MONITOR'S REPORT NUMBER(S)	
12. DISTRIBUTION/AVAILABILITY STATEMENT APPROVED FOR PUBLIC RELEASE; DISTRIBUTION UNLIMITED					
13. SUPPLEMENTARY NOTES					
14. ABSTRACT <p>The structure and time development of the magnetosphere-ionosphere system have significant impacts on the Air Force and its mission. Specifically, an accurate knowledge of ionospheric plasma densities is important for the operation of many Air Force systems. This research analyzes plasma density structure development through comparing two distinct electric field models.</p> <p>The two models compared here are a commonly used statistical model created by Heppner and Maynard [1987], and a more recently developed model using real-time coherent radar measurements from the SuperDARN radar network. Ionospheric simulations were run using Utah State University's Time-Dependent Ionospheric Model (TDIM) with the two electric field models as drivers, and density results from the simulations were compared with both a conceptual model and in-situ DMSP satellite measurements.</p> <p>While there are limitations to the comparison technique, results indicate that, in general, using the SuperDARN-derived electric fields to drive the TDIM has advantages over using the statistical fields. The higher spatial and temporal resolution of the input electric fields generally seem to produce more realistic morphological density structures, with smoothing due to statistical averaging and geomagnetic index-binning reduced. This research provides an essential first step in using high resolution, real-time SuperDARN-derived electric fields to drive a physical model of the ionosphere in order to create realistic ionospheric density results.</p>					
15. SUBJECT TERMS Ionosphere, Electric Field, Ionospheric Convection, SuperDARN, Ionospheric Modeling					
16. SECURITY CLASSIFICATION OF:			17. LIMITATION OF ABSTRACT	18. NUMBER OF PAGES	19a. NAME OF RESPONSIBLE PERSON
REPORT U	ABSTRACT U	c. THIS PAGE U			Clark E. Groves, Maj, USAF (ENP)
					19b. TELEPHONE NUMBER (Include area code) (937) 255-3636, ext 4505; e-mail: clark.groves@afit.edu

Standard Form 298 (Rev: 8-98)

Prescribed by ANSI Std. Z39-18